Accepted Manuscript

Geological Society, London, Special Publications

Grain-Size Analysis of the Late Pleistocene Sediments in the Corinth Rift: Insights into Strait Influenced Hydrodynamics and Provenance of an Active Rift Basin

Wenjun Kang, Shunli Li, Robert L. Gawthorpe, Mary Ford, Richard E. Ll. Collier, Xinghe Yu, Liliane Janikian, Casey W. Nixon, Romain Hemelsdaël, Spyros Sergiou, Jack Gillespie, Sofia Pechlivanidou & Gino De Gelder

DOI: https://doi.org/10.1144/SP523-2022-166

To access the most recent version of this article, please click the DOI URL in the line above. When citing this article please include the above DOI.

Received 19 May 2022
Revised 12 October 2022
Accepted 12 October 2022

Grain-Size Analysis of the Late Pleistocene Sediments in the Corinth Rift: Insights into Strait Influenced Hydrodynamics and Provenance of an Active Rift Basin

Wenjun Kang[1], Shunli Li[1※], Robert L. Gawthorpe[2], Mary Ford[3], Richard E. Ll. Collier[4], Xinghe Yu[1], Liliane Janikian[5], Casey W. Nixon[2], Romain Hemelsdaël[6], Spyros Sergiou[7], Jack Gillespie[8], Sofia Pechlivanidou[2], Gino De Gelder[9].

[1]School of Energy Resources, China University of Geosciences, Beijing, China

[2]Department of Earth Science, University of Bergen, Norway

[3]Université de Lorraine, ENSG, INP, France

[4]School of Earth and Environment, University of Leeds, United Kingdom

[5]Universidade Federal de São Paulo, Rua Carvalho de Mendonça, Brazil

[6]Géosciences Montpellier, Université de Montpellier, France

[7]Department of Geology, University of Patras, Greece

[8]Center for Tectonics, Resources, and Exploration (TRaX), Department of Earth Sciences, School of Physical Sciences, University of Adelaide, Australia

[9]Institut de Physique du Globe de Paris, Sorbonne Paris Cité, Université Paris Diderot, France

Present addresses: No.29, Xueyuan Road, Haidian District, School of Energy Resources, China University of Geosciences, Beijing, 100083, China

[※]Corresponding author (e-mail: lishunli@cugb.edu.cn)

Abstract

Grain-size analysis of the sediments in borehole M0079A, which is located in the Corinth Rift, was used to explore hydrodynamic conditions and provenance in the Late Pleistcene Corinth Rift. Grain-size populations that were sensitive to the sedimentary environments were characterized by frequency distribution, particle size-standard deviation, and probability cumulative curves. Our results indicate the grain-size population component in the range 0.15-0.25 μm may be used as a sensitive proxy for hyperpycnal flows, which have commonly been triggered by river floods from the southern margin of the rift since ca. 0.593-0.613 Ma. The high-density plumes derived from the longer rivers of the southern rift that were prevalent before ca. 0.593-0.613 Ma. When sediment is supplied as hemipelagic deposition, the proportion of the total grain-size population that is in the 0.3-0.5 μm range becomes an index for suspension fall-out deposits. The core shows coarser sediments during the marine periods and this may be linked to the current circulation related to the Ishtmia Strait opening. The study thus illustrates how the establishment of interbasinal straits can influence the details of sedimentary hydrodynamics in the deep-water axis of an adjacent depocenter.

Keywords: sensitivity population; strait opening/closure; event deposits; hemipelagic; hyperpycnal flows; sedimentary environments;

Grain-size analysis provides information about transportation history, source and depositional conditions (Folk and Ward, 1957; Bui et al., 1990; Singh et al., 2007; Mir and Jeelani, 2015; Allen et al., 2016; Singh et al., 2020). Early contributions are largely the grade of grain-size by Udden (1898, 1914), Grabau (1904) and Wentworth (1922). Then, Trask (Woodford, 1933) and others (Krumbein and Pettijohn, 1938; Otto, 1939) applied various statistical coefficients to characterize the size-frequency distribution of clastic sediments (Sahu, 1964). In the 1950s and 1960s, grain-size analysis was widely used in the identification of hydrodynamic conditions and as the basis for facies analysis (Passega, 1957; Mason and Folk, 1958; Fuller, 1961; Sahu, 1964; Friedman, 1967; Visher, 1969). Grain-size analysis has come a long way in sedimentology, including here the McLaren (1985) method to predict sedimentary paths (transport directions). Since the 1990s, despite the representation and application of methods of grain-size analysis, data in geology have remained at the level of several decades ago, whilst some scholars still put forward new grain-size indexes and methods, such as particle size ratio (Ding et al., 1991), sensitive components (Xiao et al., 2006), fractal dimension (Tyler and Wheatcraft, 1992), particle size trend analysis (Gao and Collins, 1994) and so on, to restore transportation history, depositional conditions, provenances and transport dynamics, paleoenvironment and paleoclimate (Yuan et al., 2011; Lu et al, 2013; Mir and Jeelani, 2015; Kanhaiya et al., 2016; Gamboa et al., 2017; Zhang et al., 2021). The method of using sediment grain-size populations to analyze the changes in sedimentary environments has been well applied in the study of oceanic shelf and continental sediments all over the world (Prins et al., 2000; Xiao et al., 2006; Mir and Jeelani, 2015; Singh et al., 2020), including the fine-grained fractions (silt and clay) of proximal strait-adjacent deposits indicate tide processes (Beelen et al., 2022), the grain-size distribution of Quaternary deep-sea sediment in the Sumba Strait is influential on organic material (Zulhikmah et al., 2020).

Grain-size plays a fundamental role in determining the spatiotemporal scales over which internal dynamics of sedimentary systems operate (Ganti, Lamb, & McElroy, 2014; Watkins et al., 2020). The accumulation of deposits under straits-controlled current amplification (Cavazza and Longhitano, 2022; Rossi et al., 2022) also contains grain-size information that reflects the dynamics of sedimentary systems. Moreover, McNeill et al. (2019) suggest that at the glacial-interglacial timescale (100's ka) climatic and

environmental change strongly affects the nature and volume of sediment within the Corinth Basin (sediment fluxes, grain-size, lithostratigraphy, etc.), and infer that: "These orbital-timescale changes in rate and type of basin infill will likely influence early rift sedimentary and faulting processes, potentially including syn-rift stratigraphy, sediment burial rates, and organic carbon flux and preservation on deep continental margins worldwide."

According to the onshore sedimentary records and offshore seismic stratigraphy, major evolution phases of the paleoenvironments in the Corinth Rift were recognized by geologists in recent years (Sachpazi et al., 2003; Ford et al., 2007; Nixon et al., 2016). The changing environmental conditions reflected by the microfossil assemblages were interpreted to arise from fluctuating eustatic sea levels with respect to the bounding sills (or straits) of the Gulf of Corinth (Bell et al., 2009; Taylor et al., 2011; Gawthorpe et al., 2018; McNeill et al., 2019). The cores recovered by IODP Expedition 381 also provide the first evidence of sea-level driven changes in paleoenvironments of an active deep-water rift basin over hundreds of thousands of years (0-750ka) (Shillington, D.J. et al., 2018). Recently, Gawthorpe et al. (2022) suggest that the height of rift segment boundaries of the Corinth Rift control the influx of marine waters from the global ocean, and discuss how the change of marine bioturbated, non-marine bedded and laminated packages are linked to the opening or closure of the basin to the open ocean. Further confirmation of the sedimentary processes/hydrodynamic changes in response to the open strait vs closed/non-strait state of the basin have been described previously (Collier et al., 2000; Scholz et al., 2007; Li et al., 2018). However, detailed discussions of what impact fluctuations between highstand marine conditions and lowstand isolated/semi-isolated conditions will have on the grain-size of sediment or what kind of grain-size populations can reflect the hydrodynamics and provenance of sediments in the Gulf of Corinth are rare (Pechlivanidou et al., 2018; Watkins et al., 2020; Gelder et al., 2021; Maffione and Herrero-Bervera, 2022).

In this contribution, we present a study of the sediments of the Late Pleistocene in the depocenter ~20 km downstream from the paleo-strait connecting the Corinth Rift, and attempt to interpret differences in the sediment supply during the gulf when periodically sea-connected and when an isolated lake with intermittent marine incursions, from the variability of sensitive populations of grain size. This work is the results of extraction of grain-size populations sensitive to the sedimentary environments based on the

frequency distribution curve, the particle size – standard deviation method, and the probability cumulative curve. We use these, together with the discussion of the implied hydrodynamic conditions and provenance, in our aim to: (i) characterize the grain-size populations of sediments under different flow processes/mechanisms; (ii) use variability of sensitive grain-size populations to identify the main hydrodynamic conditions and provenances within the Late Pleistocene active rift, and (iii) discuss the controls of close/open (non-strait/strait) states on basin floor sedimentation and provenance evolution in the Corinth Rift. In other active rift basins that were controlled by straits with interacting processes in varying marine and non-marine environments (e.g., the Red Sea. Hussain et al., 2022), sedimentation and grain-size characteristics of sediment show similarly complicated features. This study will provide insights into the variability of hydrodynamics and provenance by analysis of sensitivity in grain-size populations.

Geological settings

The Corinth active rift, geographically located in Greece in the north-eastern Mediterranean Sea (Fig. 1a), is one of Europe's most seismically active areas, accompanied by rapid and local crustal stretching. Current extensional rates reach 10-15 mm/yr (Clarke et al., 1998; Briole et al., 2000; Bernard et al., 2006). Structurally, it is located between the North Anatolian Fault and the Kephalonia Fault/Greek subduction zone (Ford et al., 2016; Gawthorpe et al., 2018) (Fig. 1a). The Corinth Rift is also a ~100×30 km high-strain band in central Greece that experiences N-S extension (Bell et al., 2009), showing the structural features of a dustpan-shaped faulted depression or asymmetric graben (Fig. 1b).

Nowadays, the eastern end of the Gulf of Corinth is connected by the Corinth Isthmus (currently a desolate highland with an altitude of 90 m (Fig. 1a) at the basin margins). The Corinth Isthmus, however, was periodically connected with the Corinth basin during periods of high sea level between 0.1-0.6 Ma (Gawthorpe et al., 2018). The western end of the Gulf of Corinth is connected to the Mediterranean Sea across the Rion Sill (60-70 m below sea level) (Fig. 1a). This sill is interpreted to have controlled the connection since at least 200 ka between the Ionian Sea and the Gulf of Corinth (Perissoratis et al., 2000; Bell et al., 2008). More recent studies show that the Rion Sill was filled by sediments of the Rodini fluvial system (see Gawthorpe et al., 2018, their figure 13b) before 0.8 Ma, and the huge delta blocked the connection between the western part of the Gulf of Corinth and the ocean. But the elimination of land

barriers and the opening of a strait is interpreted to have occurred since 0.6 Ma at the western end (Gawthorpe et al., 2018). Meanwhile, due to the influence of glacial and interglacial periods, the fill of the Corinth Rift has experienced continental, lacustrine and marine/lacustrine alternating phases in its evolution (Ford et al., 2013).

The earliest known syn-rift sediments (ca. 3.6-4 Ma) within the Corinth Rift outcrop onshore (Collier and Dart, 1991; Collier and Thompson, 1991; Bell et al., 2009), while offshore basins equivalent to the early syn-rift deposits exposed in northern Peloponnesos were either not deposited or preserved as far north as the present rift, or they were thin and pinched out northwards at this period (Nixon et al., 2016). Nixon and others (Nixon et al., 2016) proposed ages for seismic stratigraphic Unit 1 (ca. 2-1.5 Ma to 0.6 Ma; see Fig. 1b) and Units 2 (ca. 0.6 Ma to present; see Fig. 1b) that correspond with age estimates for the onshore Middle Group and Upper Group (Rohais et al., 2007; Leeder et al., 2012; Ford et al., 2013), respectively. Around 0.8 Ma, the overall migration of fault activity in the basin was northward, but major faults bounding the Corinth Basin (largely beneath the present-day Corinth Isthmus) were largely inactive in this period, creating local depocenters and highs (Collier and Dart, 1991; Collier and Thompson, 1991; Gawthorpe et al., 2018), and the main depocenter of the Corinth Gulf continues to deepen to the west of the Isthmus. With the northward migration of the fault activity, N-dipping faults occupy a dominant position in controlling the basin subsidence (except in the western basin) (Nixon et al., 2016). By this time, the main rift depocenter has become narrower, forming the modern asymmetric graben or half-graben (Fig. 1b) (Bell et al., 2008; Gawthorpe et al., 2018).

Site M0079A in the Gulf of Corinth, the focus of observations in this paper, is located between the Corinth Isthmus ~30 km to the southeast and the Rion Sill ~80 km to the northwest (Fig. 1a). The sediments recovered from site M0079A may be derived from southern fluvial systems, deltas, turbidity currents and hemipelagic suspension (Bell et al., 2008; Ford et al., 2016; Gawthorpe et al., 2018). Since 0.8 Ma, the water depth has seen a relative deepening trend (i.e., deepening events; Ford et al., 2016), due to the fluctuation of sea level relative to the boundary of the basin (Perissoratis et al., 2000), ongoing background hanging wall subsidence, and the apparently fortuitous elevation of horst blocks at basin margins (Piper et al., 1988), and migration of faults (Collier and Dart, 1991; Ford et al., 2016).

Materials and chronological framework

Data and methods

Sediments sampling and grain-size measurements

The research datasets come from the Corinth Active Rift Development IODP Expedition 381. This study focuses on the sampling of the 249-323 mbsf and 540-630 mbsf intervals of hole M0079A, a collection of 111 samples. Samples were extracted from the M0079A cores at the spacing of 0.5 to 2 m, and the length of a single sample is 2 cm.

The grain-size measurements were carried out on the Mastersizer 2000, which is made by Malvern Company of the United Kingdom. It measures in the range of 0.02-2000 μm and can provide the volume percentage content of each particle size component. The grading standard followed the Udden-Wentworth grade scale (Udden, 1914; Wentworth, 1922). Grain-sizes were represented by the φ value (Krumbein, 1934). Grain-size parameters (i.e., particle size, standard deviation and skewness; later in this article) were calculated using the formulas of McManus (1988). The detailed pre-processing of the grain-size analysis sample was as follows: (1) 10% H_2O_2 was added to remove organic matter and soluble salt (NaCl, KCl et al., in seawater) from the sediment; (2) 10% HCl, was added to remove carbonate cements, then distilled water is added and left for more than 12 hours; (3) 10% sodium hexametaphosphate was added and fully dispersed in an ultrasonic oscillator; (4) the treated sediment was put into a beaker containing distilled water, and the sediment was pumped into the laser particle size analyzer through high-speed blades; (5) the particle size data were obtained on the computer connected to the laser particle size analyzer.

Source of reference data

The X-ray fluorescence (XRF) measurements were carried out on the XRF-scanner in MARUM (Universit y of Bremen) and the data of XRF are new in this paper. Preliminary methods and results of the XRF data of IODP Expedition 381 are accessible on https://iodp.pangaea.de/front_content.php?idcat=616&count=10 &q=citation%3A%22X-Ray%20fluorescence%20(XRF)%20scanning%22.

In order to better use data of the XRF, all the key element intensities were calibrated against 16 representative samples taken from the 249-323 mbsf and 540-630 mbsf intervals of hole M0079A. The LRCE-based calibration undertaken for the study section involved additive log transformation (alr) of

intensity and concentration data following Weltje & Tjallingii (2008) and Hussain et al. (2020). The original data on element intensity and concentration were obtained during IODP Expedition 381. Regression analysis showed tight correlations between intensity and concentration for the majority of elements as indicated by high R2 values (typically >0.98; see calibration in Fig. 2a). Based on the goodness-of-fit (highest R2 value with the maximum number of elements), Ca was selected as an optimum denominator for the calibrated log ratio data (see inset data table in Fig. 2b, 2c, and 2d).

Calcareous nannofossils, non-marine diatoms and benthic foraminifera were counted from core catcher samples offshore and examined at approximately 5-m intervals. Qualitative counts data of calcareous nannofossils and non-marine diatoms were from McNeill et al. (2019), which were based on the Cascading Count Method (Styzen, 1997), with specific counting criteria available in the paper of McNeill et al. (2019).

Grain-size populations

To separate a single grain-size population from all frequency distribution curves, this paper uses the standard deviation-particle size method (Sun et al., 2002; Xiao et al., 2006), which is more sensitive to fine populations, and obtains the number and distribution range of sensitive grain-size populations. For each 100 particle size classes given by the Mastersizer 2000, the standard deviation of 111 samples was calculated, and the relationship between standard deviation and particle size is outlined in the section on sensitivity populations.

In this paper, the probability accumulation curve was used for the first time for extracting the grain-size populations sensitive to environmental changes. The probability accumulation curve was drawn with reference to the standard probability curve plate of Visher (1969), in which the extended abscissa 4.5-8.5 φ segment was added to better reflect the grain-size characteristics of sediments in the study area.

Age model

The boundary age of the M0079A subunit in this study was obtained by Maffione and Herrero-Bervera (2022), using magnetostratigraphic and relative paleointensity (RPI) constraints from 885 discrete samples from International Ocean Discovery Program (IODP) Hole M0079A to generate an unprecedented high-resolution (~15 kyr) age model for the youngest part of the Corinth's offshore syn-rift sequence.

Description of the drilled cores

Intervals of 265.84-269.31 mbsf, 270.885-275.435 mbsf, 298.14-307.92 mbsf and 540-544 mbsf were interpreted as marine deposits, while intervals of 249-265.84 mbsf, 269.31-270.885 mbsf, 275.435-298 mbsf, 307.92-323 mbsf and 544-558.29 mbsf were attributed to isolated/semi-isolated lake deposits. The interval of 558.29-630 mbsf was interpreted as intermittent marine incursion deposits.

Isolated/semi-isolated sedimentary environments

The bulk of the deposition within the isolated/semi-isolated sediment succession was composed of light grayish-green mud shale and gray-white calcareous argillaceous siltstone. The latter were intercalated in the transition zone between non-marine (i.e., isolated/semi-isolated) and marine formations (Fig. 3 and Fig. 4), indicating episodic confinement within a lacustrine system (Moretti et al., 2004). Gray-white calcareous argillaceous siltstone was interpreted as chemical deposition of aragonite in an oversaturated environment (Moretti et al., 2004; Lykousis et al., 2007). Non-marine diatoms that reflect the isolated/semi-isolated conditions (McNeill et al., 2019) occurred in intervals of 249-265.84 mbsf, 269.31-270.885 mbsf, 275.435-298 mbsf, 307.92-323 mbsf and 544-558.29 mbsf, where trace fossils such as *Teichichnus* and *Phycosiphon* appear at the same time. *Teichichnus* (Fig. 5) commonly are found in lower shoreface to offshore environments associated with the Cruziana ichnofacies (Pemberton et al., 2009). *Phycosiphon* (Fig. 5) reflects isolated basins or semi-enclosed lagoons and bays (Jiang, 2010).

Among the geochemical indices, the enrichment of Sr is often related to the aragonite needles occurring more frequently within the (semi-)isolated interval than in the marine interval, especially in the transition from marine to (semi-)isolated environments (McNeill et al., 2019; Gelder et al., 2021). Sr was enriched at 265 mbsf, 269 mbsf, 271 mbsf, 276 mbsf, 298 mbsf, 307 mbsf, 542 mbsf, 544 mbsf and 588-592 mbsf, and most of the sediments were gray-white calcareous argillaceous siltstone (Fig. 3 and Fig. 4). The gray-white calcareous argillaceous siltstone was interpreted as chemical precipitation in the water column of an evaporitic lake (Moretti et al., 2004). The Mg partition coefficient in calcite decreases with increasing salinity, and the partition coefficient of Sr in aragonite is unaffected by salinity variations ((Zhong and Mucci, 1989). The enrichment of Sr, thus, is an indicator of the end and early stage of marine or isolated/semi-isolated conditions.

Ca and the Ca/Sr ratio show a consistent trend, presenting high values in the 249-265.84 mbsf, 269.31-270.885 mbsf, 275.435-298 mbsf, 307.92-323 mbsf and 544-558.29 mbsf intervals (Fig. 3 and Fig. 4; indicated by the black solid arrow), whereas Mn and Br show low values in the same intervals. Freshwater influx during the transitional stages of semi-isolated conditions induced salinity decrease of the water. Incorporating riverine Sr influx, precipitation rates of aragonite would increase significantly when salinity decreased (Zhong and Mucci, 1989; Bickle et al., 2005). Subsequently, decreasing atmospheric CO_2 and an increase of carbonate erosion onshore (Nizou et al., 2010; Shillington et al., 2019, McNeill et al., 2019) during glacial periods drove supersaturation of dissolved CO_3^{2-} and Ca^{2+} in the Corinth Rift, which resulted in the enrichment of Ca in the 249-265.84 mbsf, 269.31-270.885 mbsf, 275.435-298 mbsf, 307.92-323 mbsf and 544-558.29 mbsf intervals (Fig. 3 and Fig. 4; indicated by the black solid arrow).

Marine sedimentary environment

The marine succession mostly consists of purplish-green siltstone with bioturbation. Between 265.84-269.31 mbsf, 270.885-275.435 mbsf, 298.14-307.92 mbsf and 540-544 mbsf, numerous calcareous nannofossils and benthic foraminifera (Fig. 3 and Fig. 4) indicated a fully marine environment (Heezen et al., 1966; McNeill et al., 2019), with some trace fossils (i.e., *Phoebichnus*, Fig. 5). *Phoebichnus* is a large, radiating trace fossil most commonly found in shallow marine siliciclastic deposits (Evans, 2016).

Mn shows high-values in the 265.84-269.31 mbsf, 270.885-275.435 mbsf, 298.14-307.92 mbsf and 540-544 mbsf intervals, and the value of Br in the middle of these intervals is higher than on either side (Fig. 3 and Fig. 4; indicated by the black dashed arrow). The dissolved Mn is interpreted to have been oxidized into MnO2 by adequate oxygen and subsequently sedimented to the sea floor (Mangini et al., 1990, Shillington et al., 2019) in interglacial periods, inducing higher values of Mn in the 265.84-269.31 mbsf, 270.885-275.435 mbsf, 298.14-307.92 mbsf and 540-544 mbsf intervals. Br-containing organic compounds are mainly formed by macro- and microalgae (Quack and Wallace, 2003). The high salinity and low temperatures could increase the production of micro-organisms (Abrahamsson et al., 2018), and contribute to forming the high concentrations of Br. The enrichment and concentration increase of Br indicates marine conditions and opening of the strait (Rion sill or/and Corinth Isthmus) (Malcolm and Price, 1984; Jiang, 2010; Caley et al., 2011).

Intermittent marine incursions

In the 558.29-630 mbsf interval, the lithofacies were mainly composed of light grayish-green mudstone, with alternations of purplish-green, grayish-white, gray-white calcareous argillaceous siltstone, light-yellow siltstone and brownish-brown gravel sandstones (Fig. 4). The intermittent occurrence of the trace fossil *Phoebichnus* (Fig. 5), in the intervals of 597-600 mbsf, 614-615 mbsf and 626-627 mbsf was accompanied by sparse calcareous nannofossils (Fig. 4). The rarity of benthic foraminifera in the interval 558.29-630 mbsf points to chronically reduced salinity (Kontopoulos and Avramidis, 2003). Fe, Br, and the Mg/Ca ratio show a periodic fluctuation with a narrow range in the 558.29-630 mbsf interval (Fig. 4; indicated by the red arrow). Br high-concentrations are directly related to the marine conditions (Malcolm and Price, 1984). Trends of Br content were opposite to that of terrigenous elements (Fe) and Mg/Ca ratio (a decline reflecting the decrease of water temperature; a rise indicating interglacial periods and marine environments; Lea et al., 2000, Shillington et al., 2019, McNeill et al., 2019) in the 558.29-630 mbsf interval.

Furthermore, according to the characteristics of the sediment in the Aliki lagoon (Gulf of Corinth) (Kontopoulos and Avramidis, 2003), we infer that the 558.29-630 mbsf interval was dominated by an isolated lake, with only intermittent marine incursions.

Grain-size features

This paper extracts the grain-size populations which may be sensitive to hydrodynamics and provenance under different environments (isolated/semi-isolated, marine and intermittent marine) of the Corinth Rift by three methods of grain-size analysis. The results show that the grain-size populations <3.9 μm (clay), 0.15-0.25 μm, 0.3-0.5 μm, <62.5 μm (clay and silt), 88.4-250.0 μm (very fine to fine sand) and 176.8-500.0 μm (fine to medium sand) were sensitive to the changes of sedimentary environments and hydrodynamic conditions in the Gulf of the Corinth.

Frequency distribution curve

The frequency distribution curves of sediments were mostly of trimodal or four peaks in the research interval of M0079A, and contain coarse and fine tails (Fig. 6b). The frequency distribution curves of

isolated/semi-isolated and marine environments cross each other, and are hard to distinguish, but the content of components of <3.9 μm is higher than that in marine environments (Fig. 6b). The multimodal character frequency distribution curve generally indicates changes of multiple provenance, transportation and dynamic conditions. From the skewness (S_k)-standard deviation (σ_φ) diagram (Fig. 6a), the sampling points of isolated/semi-isolated are in the range of -0.13 <S_k <0.83, 2.49 <σ_φ <3.27, the sampling points of marine are in the range of -0.34 <Sk <0.48, 2.46 <σφ <3.54, the sampling points of intermittent marine are in the range of -0.27 <Sk <0.74, 2.34 <σφ <3.78, and the sorting is poor, nearly symmetrical and positive. The sorting and skewness of sampling points in marine and intermittent marine are similar, and nearly symmetrical, indicating that the sediment was mixed with many components, and the coarse-grained and fine-grained components are approximately equal. However, the sorting and skewness of sampling points are concentrated in isolated/semi-isolated, and positive is dominant, indicating that the coarse-grained components are dominant for sediment.

In addition, all the frequency distribution curves have a partially similar trend (Fig. 6b). This trend was clay fraction (<3.9 μm), with two main peaks, which may reflect the influences of single provenance and multi-hydrodynamic conditions on clay fraction (for example, the trend may indicate a single provenance of a river, with high-density plume or hyperpycnal flows triggered by floods, and other transportation). However, the curve trend (>3.9 μm) was random with respect to the curve trend (<3.9 μm), which may indicate a more complex mix of sources and/or depositional processes. Therefore, this section only selects the clay fraction (<3.9 μm) as an index for the sensitivity population.

Sensitivity populations

Several peaks and troughs were observed in Fig. 7. In three curves of standard deviation vs. particle size for core M0079A samples, the trimodal grain-size interval ranges with similar trends were 0.15-0.25 μm, 0.6-0.9 μm and 3-5.5 μm, respectively (Fig. 7). They have higher standard deviations, especially in the range of 0.15-0.25 μm (Fig. 7), which represents a population of grains with the highest variability through time (Xiao et al., 2006). In contrast, two troughs, at 0.3-0.5 μm and 0.9-1.5 μm particle size intervals (Fig. 7), have low standard deviations, which indicate that these ranges of the grain-size population do not change importantly in all the samples of sediment. In the sensitivity curves at particle sizes > 0.5 μm (Fig. 7), there are no visible differences between the peak and trough values. Therefore, grain-size populations

of 0.15-0.25 μm and 0.3-0.5 μm were selected with reference to the maximum and minimum value of standard deviations in this paper.

Probability cumulative curve

The coarse and fine cut-off points reflect the significant change of the material size distribution in the two-section type (Fig. 8c) and three-section type (Fig. 8d) formula (Lin et al., 2005), and the zero-section type (Fig. 8a) content (<62.5 μm) was extracted into grain-size populations, these being sensitive to environmental changes and, specifically, to transport process as outlined below.

The probability cumulative curve types of borehole M0079A were mainly divided into four types: zero-section type (i.e., with particle size less than suspension populations), one-section type (i.e., suspension populations), two-section type (i.e., saltation and suspension populations) and three-section type (i.e., traction, saltation and suspension populations), showing little discrimination for different environments in the study sections. The shape of the zero-section type probability cumulative curve exceeds the standard probability cumulative curve chart (Fig. 8a), which shows all of the sediments represent a suspended load population. Similarly, the one-section type probability cumulative curve, like a straight line (Fig. 8b), indicates that almost all of them were suspension populations. The proportion of the suspended load population is about 98% in the two-section type and is about 90% in the three-section type. The results show that the probability cumulative curve of all samples describes a mainly suspension population with a size of less than 62.5 μm.

The probability cumulative curve of the two-section type was also composed of a saltation population and a suspension population (Fig. 8c). Compared with the two-section type curve, the probability cumulative curve of the three-section type has more of a traction population (Fig. 8d). Whether it is two-section or three-section type, the range of the fine cut-off point is roughly between 2.0-3.5 φ. This grain-size population represents the coarsest particles that can be suspended, indicating the transition between transportation modalities (i.e., the size of a sediment particle that maybe held in suspension is dependent upon turbulence), and reflects the change in the size distribution of the wash load or material transported dominantly in suspension (Lane, 1938; Visher, 1969). In contrast, the range of the coarse cut-off point is between 1.0-2.5 φ in the three-section type, which represents the coarsest particle that can jump. This transition has been attributed by some workers as the junction between the Stokes and Impact Law

formulae (Fuller, 1961; Visher, 1969), and this might be interpreted as the size where inertial forces cause rolling or sliding of particles rather than saltation (Visher, 1969). However, saltation and traction populations are difficult to transport beyond the shoreface region unless there are vigorous bottom currents (e.g., ocean-bottom currents, hyperpycnal flows, contour currents, etc.) or other trigger mechanisms (e.g., seismic, volcanic activity, tsunami wave, monsoon flooding, etc.).

Discussion

Interpretation of the grain-size populations

Centimeter-thick sand layers and homogeneous mud (e.g., Fig. 10, 79A-9) were observed in the cores with variation in population content at <3.9 μm, 0.15-0.25 μm, 0.3-0.5 μm, <62.5 μm, 88.4-250.0 μm and 176.8-500.0 μm (e.g., at 259.9 mbsf, 540.67mbsf and 565.23 mbsf). Origins and trigger mechanisms of these sedimentary events in the Gulf of Corinth may include seismically induced gravitational mass flows (Nomikou et al., 2011; Sergiou et al., 2016), earthquake-triggered tsunamis (Stefatos et al., 2006), gravitational collapse-initiated gravity flow in ancient deltas along the southern margin (Backert et al., 2010; Gawthorpe et al., 2017; Fig. 9, a-1 and a-2), and density flows in the modern submarine canyons (McNeill et al., 2005) of the Gulf of Corinth. These flows might be enhanced by fluxes of sediment from the strait (Collier and Thompson, 1991), contributing to the delivery of shallow sediments to the deep-water basin axis. Seismicity may be the primary controlling factor of these sedimentary events (Gelder et al., 2021; Gawthorpe et al., 2022), taking into account the Corinth Rift is one of Europe's most seismically active areas (McNeill et al. 2019) and the characteristics of some sedimentary events have allowed the interpretation of earthquake-induced deposits from cores in the central part of the Corinth Rift (Campos et al., 2013). In addition, the probability accumulation curves of the samples of event deposits (i.e., 79A-9, 79A-56, 79A-73; Fig. 10) are mainly three-section type types (Fig. 10), and the proportion of the total content of saltation and traction populations is more than 20% (Fig. 10), which need vigorous slope parallel bottom currents to transport. The main characteristics of the event deposits were as follows (Fig. 10): a peak in the 0.3-0.5 μm population component, a decrease of population content at 0.15-0.25 μm, a relatively significant increase of population content at the coarse and fine cut-off points, and a visible decrease of the <3.9 μm and <62.5 μm population components.

Sedimentary structures representing wave actions were not observed in the cores (e.g., at 288.00 mbsf, 289.13 mbsf, 314.78 mbsf, 544.37 mbsf, 600.34 mbsf; Fig. 10) which suggests this site (Fig. 1a) was located at a depth beyond the reach of sea or lake waves during this period. The content of the grain-size population of 0.3-0.5 μm from the 249-323 mbsf section (Fig. 10) has only one larger peak at 259.9 mbsf and was stable at about 0.8% in the rest of the section. According to the known environmental background (see Fig. 3 and Fig. 4; Bell et al., 2009; Gawthorpe et al., 2018), the results indicate that the change of the content of this population of 0.3-0.5 μm was almost unaffected by the alternation of marine and isolated/semi-isolated (i.e., continental) environments. Therefore, this content of the grain-size population from 0.3-0.5 μm was maintained at 0.8%, which was likely to represent the suspended deposits under extremely low-energy, perhaps as an indicator of hemipelagic deposit (provenance 1) as detailed in the next section.

The population content of 0.15-0.25 μm grains was zero (Fig. 10) in some sections (e.g., between 275 mbsf and 290 mbsf), with the probability accumulation curves of samples mainly one-section type and zero-section type (Fig. 10), and the proportion of the finer-grained particles ($\varphi > 3$) was more than 99% (Fig. 10). The core was dominated by massive mudstone without recognizable bedding near the sampling location (Fig. 10; see 79A-29, 79A-30, 79A-49, etc.). The population content of the coarse and fine cut-off points within these samples is also near zero (Fig. 10), implying the sediments in this site (Fig. 1a) were deposited from suspension during this time. This is supported by modern sedimentation within the Gulf, where mud (silt and clay) dominates (>95%) the deeper water (> 100 m) parts of the northern continental shelf (Poulos et al., 1996).

Weak and dilute flows generated by currents most likely deposited thin and fine-grained sediment layers (mm to <10 cm; e.g., 580.05 mbsf, 589.19 mbsf, 605.09 mbsf, 619.26 mbsf; Fig. 9, b-1 and b-2; Fig. 10). The content of the grain-size population in the range 0.3-0.5 μm from the 540-630 mbsf section fluctuates greatly (except 540-573 mbsf section) compared with that of the 249-323 mbsf section (Fig. 10). A peak (at 259.9 mbsf) in the proportion of 0.3-0.5 μm grains in the 249-323 mbsf section was similar to observations at 540.67mbsf and 565.23 mbsf (Fig. 10), consistent with the grain-size characteristics of event deposits. The fluctuation in the 0.3-0.5 μm grain size component in the 573-630 mbsf section was different from the typical grain-size population of event deposits and from the grain-size population at 0.3-

0.5 μm whose content is stable at 0.8% in the 249-323 mbsf section. Therefore, the fluctuation of the 0.3-0.5 μm grain size component in the 573-630 mbsf section is interpreted to have been caused by a high-density plume (hydrodynamics 1) derived from fluvial discharge (provenance 2) (as detailed in the next section).

On the other hand, the proportion of the grain-size population in the range 0.15-0.25 μm was relatively stable at ca. 10% in the 573-630 mbsf section, while also occasionally reaching 10% in the 249-323 mbsf and 540-573 mbsf sections (the remaining interval content was zero) (Fig. 10). Simultaneously, the population content of the coarse and fine cut-off points show frequent small changes at the same core-depth locations (i.e., where the 0.15-0.25 μm content is at about 10%) (Fig. 10). The probability accumulation curves of samples with variations in the 0.15-0.25 μm population content (more than 10%) in the study section were calculated (e.g., 79A-11, 79A-38, 79A-58, 79A-82, 79A-87, 79A-95, 79A-104; Fig. 10), mainly in three-section type and two- section type (Fig. 10). The total content of saltation and traction populations accounts for <10% (Fig. 10), clearly distinguishable from the grain-size characteristics of event deposits (Fig. 10). From these results, we have inferred that hyperpycnal flows (hydrodynamics 2) existed in the study area, which derived from fluvial flood discharge (provenance 3) (as detailed in the next section). These inferred hyperpycnal flows may have provided the stable sediment supply in the 573-630 mbsf section, and the intermittent sediment supply in the 249-323 mbsf and 540-573 mbsf sections. The latter hyperpycnal flows from fluvial flood discharge might have been controlled by the current circulation related to the Ishtmia Strait opening.

Hydrodynamics and sediment provenance change

Fluxes and contributions of main sources to the Gulf of Corinth sediment were complex (e.g., Bell et al., 2009; Nixon et al., 2016; Gawthorpe et al., 2018). In source-to-sink studies for the Corinth rift, Pechlivanidou et al. (2019) argued that the deposited sediments are sands, silts, and clays generated by fluvial erosion of the rift margins for the past 130 ka. Several studies agreed (Collier and Thompson, 1991; Lykousis et al., 2007; Bell et al., 2008; Ford et al., 2016; Gawthorpe et al., 2018) that the sediments may be derived from southern fluvial systems, deltas, gravity deposits, hemipelagic suspension and the flux of sediment from the strait. On the south of the Gulf of Corinth, conglomerate sheets and channel bodies within background sediments of mudstone, siltstone and sandstone are observed in outcrops which expose

parts of the Corinth Rift Pleistocene stratigraphy (Gawthorpe et al., 2017). It is thus reasonable that the eastern (including Corinth Isthmus) and central Gulf of Corinth catchments could provide material for the development of hyperpycnal flows and plumes.

From Unit 2 onwards, nearly all sedimentation was concentrated in the Gulf and most probably consisted of predominantly fine-grained prodelta facies and hemipelagic deposits (Ford et al., 2016). Several rivers were reversed to a southward flow direction by rapid footwall uplift, starting early in the 700-400 ka time interval (Demoulin et al. 2015), such that the eastern rift is relatively sediment-starved (sediment was supplied from the south by short, consequent rivers; Demoulin et al., 2015), with bathymetry increasing eastwards to over 800 m (Ford et al., 2016). Modern sedimentation within the Gulf is controlled by the input of terrigenous material (by ephemeral rivers and streams along the coastline (Poulos et al., 1996). Hemipelagic processes are associated with biogenic debris from the water column (Poulos et al., 1996) because the biogenic debris includes calcareous algae, benthic foraminifera, ostracods, gastropods, bivalves, dentalium, echinoids and planktonic foraminifera. At the site of M0079A, as can be inferred from the above studies (Fig. 10 and Fig. 11), a stable sediment supply of hemipelagics has operated for the past 700 ka, the suspended load grain-size population tending to be stable, especially since the decrease of river sediment due to drainage reversal (Fig. 11). The hemipelagic deposits (i.e., provenance 1, Fig. 9, c-1 and c-2) are inferred where the 0.3-0.5 μm grain-size population is maintained at 0.8%, and so in the Corinth Rift we interpret this as an index that represents hemipelagic deposition.

Cumulative seasonal erosion potential experiments (Leeder et al., 1998) predicted enhanced sediment yields for a cool, wet winter climate during full-glacial climate conditions, and reduced yields for a cool, dry winter climate during interglacial climates. Collier et al. (2000) reported latest Quaternary highstand deposits are distinguished from lowstand Lake Corinth deposits on the basis of seismic reflection data and micropaleontological and palynological analyses of drop cores, and demonstrated enhanced seasonality during the glacial period, with cool, dry summer and wet winter conditions in the Gulf of Corinth. McNeill et al. (2019) reported that the significant increase in sediment fluxes of Lake Corinth during the glacial/isolated periods was confirmed by the IODP core-based sedimentation rates. The above illustrated that rivers maintained effective runoff values of a year during full-glacial conditions because of reduced summer evaporation and increased winter precipitation (Collier et al., 2000). Interglacial conditions were

just the opposite. In the site of M0079A, however, little sediment is supplied from the north as no significant rivers flow into the Gulf from the northern coastline (Demoulin et al., 2015; Gawthorpe et al, 2018) and mainly fine-grained sediment is supplied from the south by short, consequent rivers (Demoulin et al., 2015; Ford et al., 2016). It is interpreted that the eastern and central Gulf of Corinth had a stable higher fluvial sediment contribution before drainage reversal (when there were larger catchments in the rift footwall), and then the fluvial sediment flux decreased significantly.

Along the southern margin of the Corinth rift, Poulos et al. (1996) suggested that gravity-driven mass flows are often generated often by high fluvial sediment contributions from seasonal rivers or freshwater flood events. Bates (1953) and others (Mulder and Syvitski, 1995; Mulder et al., 2003) indicated that the high-density plumes triggered by river floods generate hyperpycnal flows. Piper et al. (1988) also indicated that the fine sediment reaching the basin floor (Gulf of Corinth) appears derived mainly from muddy plumes during winter floods. These studies revealed that fluvial sediments could be transported to the basin floor during flood events. This was supported by recent research within the Gulf (Maffione and Herrero-Bervera, 2022), recognizing that the variability in grain-size may have been related to the variable intensity of bottom currents in the rift basin.

In addition, Ford et al. (2016) built a model of the westwards propagation and northwards migration of the rift since the Pleistocene, and a recent deepening event that occurred in the central Gulf of Corinth at approximately 400 ka. This deepening event was similar to the understanding of some workers (Lykousis et al., 2007) in which the present-day depth of the central Gulf of Corinth seafloor (870 m) could be the result of a continuous deepening of the basin during the last 500 ka. These show that the water depth of hole M0079A deepens since ca. 400-500 ka.

The above studies imply a relatively sustained sediment supply from rivers (i.e., high-density plumes) during the interval 700 ka to circa 500-400 ka. Since circa 400-500 ka, fluvial sediments were transported to the study area during floods (i.e., as hyperpycnal flows) during the continuous deepening of the basin. The variation of sediment supply from rivers is denoted by the variation in the 0.15-0.25 μm population component (Fig. 11) (i.e., provenance 2, fluvial discharge; hydrodynamics 1, high-density plume in the 573-630 mbsf section; and provenance 3, fluvial flood discharge; hydrodynamics 2, hyperpycnal flows in the 249-323 mbsf and 540-573 mbsf section).

The reasons for the significant changes in the content characteristics of the grain-size population at 0.15-0.25 μm and 0.3-0.5 μm in the section above and below 573 mbsf (ca. 593-613 ka) were as follows: (1) several rivers were reversed by rapid uplift starting at the beginning of the 700-400 ka interval (Demoulin et al. 2015), (2) fine-grained sediment was supplied from the south by short, consequent rivers since circa 500-400 ka (Demoulin et al., 2015; Ford et al., 2016), (3) the westwards propagation and northwards migration of the rift since the Pleistocene (Ford et al., 2016), a continuous deepening of the basin during the last 500 ka (Lykousis et al., 2007), and (4) structural subsidence and opening of straits through the pre-existing land barriers at the eastern (Corinth Isthmus) and/or western (Rion Sill) end of the Corinth Rift since approximately 0.6 Ma (i.e., the "Great Breaching" of Gawthorpe et al, 2018).

The main grain-size characteristics that allow provenance and hydrodynamic identification in this area were obtained by combining provenance, hydrodynamic analysis, probability accumulation curve and grain-size populations (Fig. 12). These may be distinguished as: (1) The probability accumulation curve of event deposits (possibly earthquake-triggered) has three-section type characteristics, with the proportion of coarse particles (<4.5 φ) close to or more than 50%, and the proportion of the total content of saltation and traction populations more than 20%. (2) The probability accumulation curve of hyperpycnal flows and high-density plumes has two-section type and three-section type characteristics, with the proportion of coarse particles (<4.5 φ) basically between 5% and 30%. The total content of saltation and traction populations accounts for <10% of the total population. (3) The probability accumulation curve of hemipelagic deposits has zero-section type and one-section type characteristics, with the proportion of the finer-grained particles (>3 φ) being more than 99%.

Central basin Late Pleistocene rift sediments recording the presence of straits

We integrate our new hydrodynamic and provenance information from the site of M0079A with published sedimentological, hydrological and new age interpretations (Maffione and Herrero-Bervera, 2022) to develop a model of the sediment supply to the site of M0079A in no-strait versus open strait states during the Late Pleistocene. The two main environmental phases of development correspond approximately to those recognized in the recent work in the central Gulf of Corinth (Nixon et al., 2016; Gawthorpe et al., 2018, McNeil et al., 2019; Gawthorpe et al., 2022):

An isolated lake with intermittent marine incursions existed from ca. 0.7 to 0.613-0.593 Ma. The main rivers of the southern catchments maintained a northward course (Fig. 1), and the site of M0079A had a stable high fluvial sediment contribution (Fig. 13b). Slumps, as isolated beds were observed in cores (Fig. 9 a-1 and a-2), indicating slopes around the site of M0079A were unstable (Fig. 13b). The deposits of high-density plumes were deposited here during this period, and accompanying slumps may have been earthquake-triggered (Sachpazi et al., 2003). At this time the presence of structural sills/land barriers at the eastern (Corinth Isthmus) and western (Rion Straits) ends of the main depocentre confined the lacustrine rift (Bell et al., 2008; Gawthorpe et al., 2018). The supply of suspended sediments was substantially derived from low-density plumes (including lofted plumes, Gawthorpe et al., 2022; Fig. 13b), with small amounts derived from hemipelagic suspension.

The main Corinth Rift depocentre was periodically sea-connected from ca. 0.613-0.593 to 0.168 Ma. The westwards propagation and northwards migration of the rift (Ford et al., 2016), cause the migration of the depocenter of the rift basin (with the deepest basin floor in the basin axis near the site of M0079A; Fig. 1; Fig. 13a). The main rivers were reversed (Fig. 1a), reducing fluvial sediment supply to the central and eastern parts of the rift. Slumps representing slope collapse deposits were not observed in cores, suggesting such deposits were trapped close to the rift margins (Fig. 13a). The deposits of this period commonly consisted of turbidites supplied by hyperpycnal flow during rivers flood events (Piper et al., 1988; Maffione and Herrero-Bervera, 2022), turbidity currents that may have been earthquake-triggered (Sachpazi et al., 2003), and the delivery of sediment from cascading strait currents off the shelf (Collier and Thompson, 1991).

Structural or erosional control of land barriers at the eastern (Corinth Isthmus) and/or western (Rion Sill) ends of the rift allowed initial marine incursion around 0.6 Ma (i.e., the "Great Breaching" of Gawthorpe et al, 2018). The sediments of shallow marine in the stratigraphic section exposed by the excavation of the Corinth Canal provide evidence for the episodic existence of a strait through much of the Late Pleistocene (Collier, 1990; Fig. 13c). Moreover, the distribution of transverse and linear dunes in the Corinth Basin suggest that a strait periodically existed across the Corinth Isthmus during the Late Pleistocene (Collier and Thompson, 1991). The oldest marine sediments exposed in the canal section occur above and then alternate with the white and grey Corinth Marls (Fig. 13c). The expression of fluctuating

relative sea level on one coastline of the Isthmus strait during this time is exemplified by the prominent karstification of a marl surface, due to a relative base-level fall (Collier, 1990). The marl is capped by a beach/shoreface transgressive to progradational package associated with glacio-eustatic marine transgression at ca. 0.4 Ma. Fig. 13d illustrates bidirectional ripples indicating tidal influence in this shallow marine environment. Tidal dune bedforms also developed within the strait during a younger glacio-eustatic transgression, as described by Collier & Thompson (1991). After each glacio-eustatic highstand, the Gulf of Corinth was cut off again from open marine conditions due to a relative base-level fall below the level of the Corinth Isthmus structural sill (Fig. 13c). Cycles of transgression and base-level fall, alternating between open and closed strait conditions, were repeated ca. every 100 ka until the Corinth Isthmus permanently emerged above sea-level (Collier, 1990), by which time marine connection during glacio-eustatic highstands was established at the western end of the rift (Somerville et al., 2019; Gawthorpe et al., 2022).

The core from the IODP borehole M0079A was collected some 10-20 km away from the Isthmia paleo-strait and associated strait currents that would have been focused through the strait during phases of relatively high sea level (Collier and Thompson, 1991). The “far field strait effect” formed by the Gulf of Corinth being periodically sea-connected might have led suspended sediments to have been mainly derived from hemipelagic suspension, from more distal the low-density plumes (Fig. 13a). However, our analysis of the deep-water core material shows the deposits got coarser during the connected (marine water) intervals (Figs. 3 and 4). This observation together with the reconstruction of the Isthmia area (Collier and Thompson, 1991) suggests that strait-related currents from the Isthmus strait likely promoted the transport of shallow water sediments into the main Corinth Rift axial depocenter from the shallower shelf. Collier and Thompson (1991) reconstructed a shallow platform in the SE part of the Gulf of Corinth basin where currents were large enough to form large bedforms. It was likely the strait currents were circulating in a clockwise pattern and were cascading off the shallow platform to deeper water, depositing coarser grained sediments and facilitating bioturbation (higher oxygen content waters). The water circulation through the structurally controlled strait and its connectivity with deep water (Fig. 13a) might explain the coarser grained deposits during accumulation of the marine deposits (Figs. 3 and 4).

Conclusions

The sedimentary environments of the Gulf of Corinth changed from an isolated lake, with intermittent marine incursions (before ca. 0.593-0.613 Ma, namely 570.51 mbsf to 577.00 mbsf), to a gulf periodically sea-connected (after ca. 0.593-0.613 Ma). In the 573-630 mbsf section, sediments were mainly derived from long rivers on the southern margin of the Corinth Rift and the fluvial-sourced sediments were transported by high-density plumes and intervening hemipelagic deposition by suspension settling. Due to drainage reversals at circa 0.593-0.613 Ma, in the 249-323 mbsf and 540-573 mbsf section, the sediments were mainly derived from hemipelagic settling and hyperpycnal flows during river (short, consequent river) flood events. Many event deposits in the study section may have been earthquake-triggered.

The 0.15-0.25 μm component of the grain-size population of the sediments in the study area (i.e., from site M0079A) was mainly deposited through hyperpycnal flows since 0.593-0.613 Ma, triggered by river floods on the southern margin of the Corinth Rift. The variation of the population content of 0.15-0.25 μm implies periodic floods. When sediment was supplied from hemipelagic deposition, the proportion of the grain-size population in the range 0.3-0.5 μm was maintained at 0.8%, which is an index that represents suspension fall-out deposits laid down under extremely low-energy conditions. Before 0.593-0.613 Ma, the 0.15-0.25 μm component of grain-size population of sediments indicates deposition out of more stable high-density plumes, sourced not far from the study area.

A probability accumulation curve chart was established to distinguish hemipelagic deposits, event deposits (possibly earthquake-triggered), hyperpycnal flows and high-density plumes in the Gulf of Corinth. This approach may be found useful in the characterization of fine-grained sediments in other deep-water settings. The deep-water sediments of the M0079A borehole record more frequent coarser beds during the marine periods when the Ishtmia Strait was open. The presence of the open strait likely changed the shallow water current circulation in the SE area of the basin and promoted delivery of shallow sediments to the deep-water basin axis.

Acknowledgments

We sincerely thank all involved with the successful completion of IODP Expedition 381, including ECORD Science Operator staff, ship and drilling crew of the D/V Fugro Synergy, and staff at MARUM, University of Bremen. We thank the Natural Science Foundation of China, Fundamental Research Funds for the Central Universities and IODP Expedition 381 provided support. We are thankful to Dr. Olariu and Dr. Rossi for editorial guidance and reviewers for insightful reviews that improved the manuscript.

Funding

This study was supported by the Natural Science Foundation of China, China (42272124, 41802129), the Fundamental Research Funds for the Central Universities, China (2-9-2019-100), and IODP Expedition 381.

Data availability

All data and material pertinent to this study are contained within the manuscript and Supplementary Information, and/or the IODP Expedition 381 Preliminary Report. The full dataset from IODP Expedition 381 will become openly available on March 1, 2019, via the IODP website (https://www.iodp.org/resources/access-data-and-samples), including access to core materials and logging data.

References

[1] Abrahamsson, K., Granfors, A., Ahnoff, M. Cuevas, C.A. and Saiz-Lopez, A. 2018. Organic bromine compounds produced in sea ice in Antarctic winter. Nat Commun 9, 5291, https://doi.org/10.1038/s41467-018-07062-8

[2] Allen, P.A., Michael, N.A., D'Arcy, M., Roda-Boluda, D.C., Whittaker, A.C., Duller, R.A. and Armitage, J.J. 2016. Fractionation of grain-size in terrestrial sediment routing systems. Basin Research, 29, 180-202, https://doi.org/10.1111/bre.12172

[3] Backert, N., Ford, M. and Malartre, F. 2010. Architecture and sedimentology of the Kerinitis Gilbert-type fan delta, Corinth Rift, Greece. Sedimentology, 57, 543-586, https://doi.org/10.1111/j.1365-3091.2009.01105.x

[4] Bates, C.C. 1953. Rational theory of delta formation. AAPG Bulletin, 37, 2119-2126, https://doi.org/10.1306/5CEADD76-16BB-11D7-8645000102C1865D

[5] Beelen, D., Wood, L.J, Zaghloul, M.N., Cardona, C. and Arts, M. 2022. Channel, dune and sand sheet architectures of a strait-adjacent delta, Rifian Corridor, Morocco. Geological Society, London, Special Publications, 523, https://doi.org/10.1144/SP523-2021-49

[6] Bell, R.E., Mcneill, L.C., Bull, J.M., Henstock, T.J., Collier, R.E.L. and Leeder, M.R. 2009. Fault architecture, basin structure and evolution of the Gulf of Corinth Rift, central Greece. Basin Research, 21, 824-855, https://doi.org/10.1111/j.1365-2117.2009.00401.x

[7] Bell, R.E., Mcneill, L.C., Bull, J.M. and Henstock, T.J. 2008. Evolution of the offshore western Gulf of Corinth. Geological Society of America Bulletin, 120, 156-178, https://doi.org/10.1130/B26212.1

[8] Bernard, P., Lyon-Caen, H., Briole, P., Deschamps, A., Boudin, F., Makropoulos, K., Papadimitriou, P., Lemeille, F., Patau, G., Billiris, H., Paradissis, D., Papazissi, K., Castarede, H., Charade, O., Nercessian, A., Avallone, A., Pacchiani, F., Zahradnik, J., Sacks, S. and Linde, A. 2006. Seismicity, deformation and seismic hazard in the western rift of Corinth: new insights from the Corinth Rift Laboratory (crl). Tectonophysics, 426, 7-30, https://doi.org/10.1016/j.tecto.2006.02.012

[9] Bickle, M.J., Chapman, H.J., Bunbury, J., Harris, N.B.W., Fairchild, I.J., Ahmad, T. and Pomiès, C. 2005. The Relative Contributions of Silicate and Carbonate Rocks to Riverine Sr Fluxes in the Head Waters of the Ganges. Geochimica et Cosmochimica Acta, 69(9): 2221-2240, https://doi.org/10.1016/j.gca.2004.11.019

[10] Briole, P., Rigo, A., Lyon-Caen, H., Ruegg, J.C. and Deschamps, A. 2000. Active deformation of the Corinth rift, Greece: results from repeated global positioning system surveys between 1990 and 1995. Journal of Geophysical Research, 105, 25605-25626, https://doi.org/10.1029/2000JB900148

[11] Bui, E.N., Loeppert, R.H. and Wilding, L.P. 1990. Carbonate phases in calcareous soils of the western united states. So il Science Society of America Journal, 54, 39-45, https://doi.org/10.2136/sssaj1990.03615995005400010006x

[12] Caley, T., Malaizé, B., Zaragosi, S., Rossignol, L., Bourget, J., Eynaud, F., Martinez, P., Giraudeau, J., Charlier, K. and Ellouz-Zimmermann, N. 2011. New Arabian Sea records help decipher orbital timing of indo-Asian monsoon. Earth &

Planetary Science Letters, 308, 433-444, https://doi.org/10.1016/j.epsl.2011.06.019

[13] Campos, C., Beck, C., Crouzet, C., Carrillo, E. and Tripsanas, E. 2013. Late Quaternary paleoseismic sedimentary archive from deep central Gulf of Corinth: time distribution of inferred earthquake-induced layers. Annals of Geophysics, 56, S0670, https://doi.org/10.4401/ag-6226

[14] Cavazza, W. and Longhitano, S.G. 2022. Palaeostrait tectonosedimentary facies during late Cenozoic microplate rifting and dispersal in the western Mediterranean. Geological Society, London, Special Publications, 523, https://doi.org/10.1144/SP523-2021-95

[15] Clarke, P.J., Davies, R.R., England, P.C., Parsons, B., Billiris, H., Paradissis, D., Veis, G., Cross, A., Denys, P.H., Ashkenazi, V., Bingley, R., Kahle, H.G., Muller, M.V. and Briole, P. 1998. Crustal strain in central Greece from repeated GPS measurements in the interval 1989–1997. Geophysical Journal International, 135, 195-214, https://doi.org/10.1046/j.1365-246X.1998.00633.x

[16] Collier, R.E.LL. 1990. Eustatic and tectonic controls upon Quaternary coastal sedimentation in the Corinth Basin, Greece. Journal of the Geological Society, 147, 301-314, https://doi.org/10.1144/gsjgs.147.2.0301

[17] Collier, R.E.L. and Dart, C.J. 1991. Neogene to quaternary rifting, sedimentation and uplift in the Corinth Basin, Greece. Journal of the Geological Society, 148, 1049-1065, https://doi.org/10.1144/gsjgs.148.6.1049

[18] Collier, R.E.L. and Thompson, J. 1991. Transverse and linear dunes in an upper Pleistocene marine sequence, Corinth Basin, Greece. Sedimentology, 38, 1021-1040, https://doi.org/10.1111/j.1365-3091.1991.tb00369.x

[19] Collier, R.E.Ll., Leeder, M.R., Trout, M., Ferentinos, G., Lyberis, E. and Papatheodorou, G. 2000. High sediment yield s and cool, wet winters: Test of last glacial paleoclimates in the northern Mediterranean. Geology, 28, 999-1002, https://doi.org/10.1130/0091-7613(2000)28<999:HSYACW>2.0.CO;2

[20] Demoulin, A., Beckers, A. and Hubert-Ferrari, A. 2015. Patterns of Quaternary uplift of the Corinth rift southern border (N Peloponnese, Greece) revealed by fluvial landscape morphometry. Geomorphology, 246, 188-204, https://doi.org/10.1016/j.geomorph.2015.05.032

[21] Ding, Z.L., Han, J.T., Liu, C., Liu, D.S. and Liu, T.S. 1991. Preliminary determination of an abrupt climatic shift around 2.5 Ma in northern China (eng). Chinese Science Bulletin, 36, 852-852, https://doi.org/10.1288/00005537-196101000-00010

[22] Evans, J.N., Mcilroy, D. and Smith, A. 2019. Ichnology and palaeobiology of phoebichnus trochoides from the middle Jurassic of north-east England. Papers in Palaeontology, 2, 139-154, https://doi.org/10.1002/spp2.1035

[23] Folk, R.L. and Ward, W.C. 1957. Brazos River bar: a study in the significance of grain-size parameters. Journal of Sedimentary Research, 27, 3-26, https://doi.org/10.1306/74D70646-2B21-11D7-8648000102C1865D

[24] Ford, M., Hemelsdal, R., Mancini, M. and Palyvos, N. 2016. Rift migration and lateral propagation: evolution of normal faults and sediment-routing systems of the western Corinth rift (Greece). Geological Society, London, Special Publications, SP439, 15, http://doi.org/10.1144/SP439.15

[25] Ford, M., Williams, E.A., Malartre, F. and Popescu, S.M., 2007. Stratigraphic architecture, sedimentology and

structure of the Vouraikos Gilbert-type fan delta, Gulf of Corinth, Greece. Sedimentary Processes, Environments and Basins: A Tribute to Peter Friend, 38, 49-90, https://doi.org/10.1002/9781444304411.ch4

[26] Ford, M., Rohais, S., Williams, E.A., Bourlange, S., Jousselin, D., Backert, N. and Malartre, F. 2013. Tectono-sedimentary evolution of the western Corinth rift (central Greece). Basin Research, 25, 3-25, https://doi.org/10.1111/j.1365-2117.2012.00550.x

[27] Friedman, G.M. 1967. Dynamic processes and statistical parameters compared for size frequency distribution of beach and river sands. Journal of Sedimentary Research, 37, 327-354, https://doi.org/10.1306/74D716CC-2B21-11D7-8648000102C1865D

[28] Fuller, A.O. 1961. Size distribution characteristics of shallow marine sands from the cape of good hope, south Africa. Journal of Sedimentary Research, 31, 256-261, https://doi.org/10.1306/74D70B4B-2B21-11D7-8648000102C1865D

[29] Gamboa, A., Montero-Serrano, J., St-Onge, G., Rochon, A. and Desiage, P. 2017. Mineralogical, geochemical, and magnetic signatures of surface sediments from the Canadian Beaufort Shelf and Amundsen Gulf (Canadian Arctic). Geochemistry Geophysics Geosystems, 18, 488-512, https://doi.org/10.1002/2016GC006477

[30] Ganti, V., Lamb, M. P. and McElroy, B. 2014. Quantitative bounds on morphodynamics and implications for reading the sedimentary record. Nature Communications, 5, 3298, https://doi.org/10.1038/ncomm s4298

[31] Gao, S. and Collins M.B. 1994. Analysis of grain-size trends, for defining sediment transport pathways in marine environments. Journal of Coastal Research, 10: 70-78, https://www.jstor.org/stable/4298194

[32] Gawthorpe, R.L., Andrews, J.E., Collier, R., Ford, M. and Skourtsos, E. 2017. Building up or out? disparate sequence a rchitectures along an active rift margin—Corinth rift, Greece. Geology, 45, 1111-1114, https://doi.org/10.1130/G39660.1

[33] Gawthorpe, R.L., Leeder, M.R., Kranis, H., Skourtsos, E., Andrews, J.E., Henstra, G.A., Mack, G.H., Muravchik, M., Turner, J.A. and Stamatakis, M. 2018. Tectono-sedimentary evolution of the Plio-Pleistocene Corinth rift, Greece. Basin Research, 30, 448-479, https://doi.org/10.1111/bre.12260

[34] Gawthorpe, R.L., Fabregas, N., Pechlivanidou, S., Ford, M., Collier, R.E.L., Carter, G.D.O., McNeill, L.C. and Shillington, D.J. 2022. Late Quaternary mud-dominated, basin-floor sedimentation of the Gulf of Corinth, Greece: Implications for deep-water depositional processes and controls on syn-rift sedimentation. Basin Research, Online, 1-34, https://doi.org/10.1111/bre.12671

[35] Grabau, A.W., 1904. Phylogeny of Fusus and its allies. Smithsonian Miscellaneous Collections, 44, 1-157.

[36] Gelder, G.D., Mai, L.D., Beck, C., Carlut, J., Seibert, C., N Feuillet, N., D.O. Carter, G., Pechlivanidou, S. and L.Gawthorpe, R. 2021. Multi-scale and multi-parametric analysis of Late Quaternary event deposits within the active Corinth Rift (Greece). Sedimentology, 69, 1573-1598, https://doi.org/10.1111/sed.12964

[37] Heezen, B.C., Ewing, M. and Johnson, G.L., 1966. The Gulf of Corinth floor. Deep Sea Research and Oceanographic Abstracts, 13, 381-411, https://doi.org/10.1016/0011-7471(66)91076-X

[38] Hussain, A., Haughton, P.D.W., Shannon, P.M., Turner, J.N., Pierce, C.S., Obradors-Latre, A., Barker, S.P. and

Martinsen, O.J. 2020. High-resolution X-ray fluorescence profiling of hybrid event beds: Implications for sediment gravity flow behaviour and deposit structure. Sedimentology, 67, 2850-2882, https://doi.org/10.1111/sed.12722

[39] Hussain, A., Butt, M.N., Olariu, C., Malik, M.H., Koeshidayatullah, A., Amao, A. and Al-Ramadan, K. 2022. Unravelling reservoir quality heterogeneity in mixed siliciclastic-carbonate deposits: An example from Miocene Red Sea rift, NW Saudi Arabia. Marine and Petroleum Geology, 145, https://doi.org/10.1016/j.marpetgeo.2022.105850.

[40] Jiang Z.X. 2010. Sedimentology (in Chinese with English abstract). Petroleum Industry Press, Beijing, pp. 237-243.

[41] Kanhaiya, S., Singh, B.P., Tripathi, M., Sahu, S. and Tiwari, V. 2016. Lithofacies and particle-size characteristics of late quaternary floodplain deposits along the middle reaches of the Ganga river, central Ganga plain, India. Geomorphology, 284, 220-228, https://doi.org/10.1016/j.geomorph.2016.08.030

[42] Kontopoulos, N. and Avramidis, P. 2003. A late Holocene record of environmental changes from the Aliki lagoon, Egion, North Peloponnesus, Greece. Quaternary International, 111, 75-90, https://doi.org/10.1016/S1040-6182(03)00016-8

[43] Krumbein, W.C. and Pettijohn, F.J. 1938. Manual of sedimentary petrography. Appleton-Century-Crofts, Inc. New York. 544.

[44] Krumbein, W.C. 1934. Size frequency distributions of sediments. Journal of Sedimentary Research, 4, 65-77, https://doi.org/10.1306/D4268EB9-2B26-11D7-8648000102C1865D

[45] Lane, E.W. 1938. Notes on the formation of sand. Eos, Transactions American Geophysical Union, 19, 505-508, https://doi.org/10.1029/TR019i001p00505

[46] Lea, D.W., Pak, D.K. and Spero, H.J. 2000. Climate impact of late quaternary equatorial pacific sea surface temperature variations. Science. 289, 1719-1724, https://doi.org/10.1126/science.289.5485.1719

[47] Leeder, M.R., Harris, T. and Kirkby, M.J. 1998. Sediment supply and climate change: Implications for basin stratigraphy. Basin Research, 10, 7-18, https://doi.org/10.1046/j.1365-2117.1998.00054.x

[48] Leeder, M.R., Mack, G.H., Brasier, A.T., Parrish, R.R., Mcintosh, W.C., Andrews, J.E. and Duermeijer, C.E. 2008. Late-Pliocene timing of Corinth (Greece) rift-margin fault migration. Earth and Planetary Science Letters, 274, 132-141, https://doi.org/10.1016/j.epsl.2008.07.006

[49] Leeder, M.R., Mark, D.F., Gawthorpe, R.L., Kranis, H., Loveless, S., Pedentchouk, N., Skourtsos, E., Turner, J., Andrews, J.E. and Stamatakis, M. 2012. A “Great Deepening”: Chronology of rift climax, Corinth Rift, Greece. Geology, 40(11), 999-1002, https://doi.org/10.1130/G33360.1

[50] Li, S., Yu, X., Steel, R., Zhu, X., Li, S., Cao, B. and Hou, G. 2018. Change from tide-influenced deltas in a regression-dominated set of sequences to tide-dominated estuaries in a transgression-dominated sequence set, East China Sea Shelf Basin. Sedimentology, 65, 2312-2338, https://doi.org/10.1111/sed.12466

[51] Lin, C.M., Zhu, H.C., Gao, S. 2005. Sedimentary facies and evolution in the Qiantang River incised valley, eastern China. Marine Geology, 219, pp. 235-259, https://doi.org/10.1016/j.margeo.2005.06.009.

[52] Lu, S.Q., Wang, J. and Cao, Y.C. 2013. Study on characteristics and hydrodynamic significance of grain-size

components of beach-bar sandbodies, second member of Shahejie formation, Chexi sag (in Chinese with English abstract). Petroleum Geology & Recovery Efficiency, 20, 26-29.

[53] Lykousis, V., Sakellariou, D., Moretti, I. and Kaberi, H., 2007. Late quaternary basin evolution of the Gulf of Corinth: Sequence stratigraphy, sedimentation, fault–slip and subsidence rates. Tectonophysics, 440, 29-51, https://doi.org/10.1016/j.tecto.2006.11.007

[54] Malcolm, S.J. and Price, N.B. 1984. The behavior of iodine and bromine in estuarine surface sediments. Marine Chemistry, 15, 263-271, https://doi.org/10.1016/0304-4203(84)90022-7

[55] Mangini, A., Eisenhauer, A. and Walter, P. 1990. Response of manganese in the ocean to the climatic cycles in the Quaternary. Paleoceanography, 5(5): 811-821, https://doi.org/10.1029/PA005i005p00811

[56] Mason, C.C. and Folk, R.L. 1958. Differentiation of beach, dune, and aeolian flat environments by size analysis, mustang island, Texas. Journal of Sedimentary Research, 28, 211-226, https://doi.org/10.1306/74D707B3-2B21-11D7-8648000102C1865D

[57] Maffione, M. and Herrero-Bervera, E. 2022. A relative paleointensity (RPI)-calibrated age model for the Corinth syn-rift sequence at IODP Hole M0079A (Gulf of Corinth, Greece). Frontiers in Earth Science, 10, https://doi.org/10.3389/feart.2022.813958

[58] McLaren, P. and Bowles, D. 1985. The effects of sediment transport on grain-size distributions. Journal of Sedimentary Research, 55, 457-470, https://doi.org/10.1306/212F86FC-2B24-11D7-8648000102C1865D

[59] McManus, J. 1988. Grain-size determination and interpretation. In: Tucker(ed). Techniques in Sedimentology. Oxford: Blackwell. pp. 63-85.

[60] McNeill, L.C., Cotterill, C.J., Henstock, T.J., Bull, J.M., Stefatos, A., Collier, R., Papatheoderou, G., Ferentinos, G. and Hicks, S.E. 2005. Active faulting within the offshore western Gulf of Corinth, Greece: Implications for models of continental rift deformation. Geology, 33, 241-244, https://doi.org/10.1130/G21127.1

[61] McNeill, L.C., Shillington, D.J., Carter, G.D.O., Everest, J.D., Gawthorpe, R.L., Miller, C., Phillips, M.P., Collier, R.E.L1., Cvetkorpe, A., Gelder, G.D., Diz, P., Doan, M.L., Ford, M., Geraga, M., Gillespie, J., Hemelsdael, R., Herrero-Bervera, E., Ismaiel, M., Janikian, L., Kouli, K., Ber, E.L., Li, S.L., Maffione, M., Mahoney, C., Machlus, M.L., Michas G., Nixon, C.W., Oflaz, S.A., Omale, A.P., Panagiotopoulos, K., Pechlivanidou, S., Sauer, S., Seguin, J., Sergiou, S., Zakharova, N.V. and Green, S. 2019. High-resolution record reveals climate-driven environmental and sedimentary changes in an active rift. Scientific Reports, 9, 6519, https://doi.org/10.1038/s41598-019-42749-y

[62] Mir, R.A. and Jeelani, G. 2015. Textural characteristics of sediments and weathering in the Jhelum river basin located in Kashmir valley, western Himalaya. Journal of the Geological Society of India, 86, 445-458, https://doi.org/10.1007/s12594-015-0332-2

[63] Moretti, I., Lykousis, V., Sakellariou, D., Reynaud, J.Y., Benziane, B. and Prinzhoffer, A. 2004. Sedimentation and subsidence rate in the Gulf of Corinth: what we learn from the marion dufresne's long-piston coring. Comptes Rendus Geoscience, 336, 291-299, https://doi.org/10.1016/j.crte.2003.11.011

[64] Mulder, T. and Syvitski, J.P.M. 1995. Turbidity currents generated at river mouths during exceptional discharges to the world oceans. Journal of Geology, 103, 285-299, https://doi.org/10.1086/629747

[65] Mulder, T., Syvitski, J.P.M., Migeon, S., Faugères, J.C. and Savoye, B. 2003. Marine hyperpycnal flows: initiation, behavior and related deposits. A review. Marine and Petroleum Geology, 20, 861-882, https://doi.org/10.1016/j.marpetgeo.2003.01.003

[66] Nixon, C.W., Mcneill, L.C., Bull, J.M., Bell, R.E., Gawthorpe, R.L., Henstock, T.J., Christodoulou, D., Ford, M., Taylor, B., Sakellariou, D., Ferentinos, G., Papatheodorou, G., Leeder, M.R., Collier, R.E.L., Goodliffe, A.M., Sachpazi, M. and Kranis, H. 2016. Rapid spatiotemporal variations in rift structure during development of the Corinth Rift, central Greece. Tectonics, 35, 1225-1248, https://doi.org/10.1002/2015TC004026

[67] Nizou, J., Hanebuth, T., Heslop, D., Schwenk, T., Palamenghi, L , Stuut, J.B. and Henrich, R. 2010. The Senegal River mud belt: A high-resolution archive of paleoclimatic change and coastal evolution. Marine Geology, 278, 150-164, https://doi.org/10.1016/j.margeo.2010.10.002

[68] Nomikou, P., Alexandri, M., Lykousis, V., Sakellariou, D. and Ballas, D. 2011. Swath bathymetry and morphological slope analysis of the Corinth Gulf. Quaternary International, 155-158.

[69] Otto, G.H. 1939. A Modified Logarithmic Probability Graph for the Interpretation of Mechanical Analyses of Sediments. Journal of Sedimentary Petrology, 9, 62-76, https://doi.org/10.1306/D4269044-2B26-11D7-8648000102C1865D

[70] Passega, R. 1957. Texture as characteristic of clastic deposition. AAPG Bulletin, 41, 1952-1984, https://doi.org/10.1306/0BDA594E-16BD-11D7-8645000102C1865D

[71] Pechlivanidou, S., Cowie, P.A., Hannisdal, B., Whittaker, A.C., Gawthorpe, R.L., Pennos, C. and Riiser, O.S. 2018. Source-to-sink analysis in an active extensional setting: Holocene erosion and deposition in the Sperchios rift, central Greece. Basin Research, 30, 522-543, https://doi.org/10.1111/bre.12263

[72] Pechlivanidou, S., Cowie, P.A., Duclaux, G., Nixon, C.W. and Salles, T. 2019. Tipping the balance: shifts in sediment production in an active rift setting. Geology. 47, 259-262, https://doi.org/10.1130/G45589.1

[73] Perissoratis, C., Piper, D.J. and Lykousis, V. 2000. Alternating marine and Lacustrine sedimentation during the late quaternary in the Gulf of Corinth rift basin, central Greece. Marine Geology, 167, 391-411, https://doi.org/10.1016/S0025-3227(00)00038-4

[74] Piper, D., Kontopoulos, N. and Panagos, A.G. 1988. Deltaic sedimentation and stratigraphic sequences in post-orogenic basins, western Greece. Sedimentary Geology, 55, 283-294, https://doi.org/10.1016/0037-0738(88)90135-2

[75] Poulos, S.E., Collins, M.B., Pattiaratchi, C., Cramp., A. Gull, W., Tsimplis, M. and Papatheodorou, G. 1996. Oceanography and sedimentation in the semi-enclosed, deep-water Gulf of Corinth (Greece). Marine Geology, 134, 213-235, https://doi.org/10.1016/0025-3227(96)00028-X

[76] Quack, B. and Wallace, D.W.R. 2003. Air-sea flux of bromoform: Controls, rates, and implications, Global Biogeochem. Cycles, 17, 1023, https://doi.org/10.1029/2002GB001890

[77] Prins, M.A., Postma, G. and Weltje, G.J. 2000. Controls on terrigenous sediment supply to the Arabian Sea during the Late Quaternary: the Indus fan. Marine Geology, 169, 351-371, https://doi.org/10.1016/S0025-3227(00)00086-4

[78] Rohais, S., Eschard, R., Ford M., Guillocheau, F. and Moretti, I. 2007. Stratigraphic architecture of the Plio-Pleistocene infill of the Corinth Rift: implications for its structural evolution. Tectonophysics, 440: 5-28, https://doi.org/10.1016/j.tecto.2006.11.006

[79] Pemberton, S.G., Gingras, J.A.M.M.K. and Bann., K.L. 2009. Trace fossil atlas: The recognition of common trace fossils in cores (short course material). pp. 1-130.

[80] Sahu, B.K. 1964. Depositional mechanisms from the size analysis of clastic sediments. Journal of Sedimentary Research, 34,73-83, https://doi.org/10.1306/74D70FCE-2B21-11D7-8648000102C1865D

[81] Sachpazi, M., Clement, C., Laigle, M., Hirn, A. and Roussos, N. 2003. Rift structure, evolution, and earthquakes in the Gulf of Corinth, from reflection seismic images. Earth and Planetary Science Letters, 216, 243-257, https://doi.org/10.1016/S0012-821X(03)00503-X

[82] Scholz, C.A., Johnson, T.C., Cohen, A.S., King, J.W., Peck, J.A., Overpeck, J.T., Talbot, M.R., Brown, E.T., Kalindekafe, L. and Amoako, P.Y.O. 2007. East African Megadroughts between 135 and 75 Thousand Years Ago and Bearing on Early-Modern Human Origins. Proceedings of the National Academy of Sciences of the United States of America, 104(42), 16416-16421, https://doi.org/10.1073/pnas.0703874104

[83] Sergiou, S., Beckers, A., Geraga, M., Papatheodorou, G. and Papaefthymiou, H. 2016. Recent sedimentary processes in the western Gulf of Corinth, Greece: seismic and aseismic turbidites. Bulletin of the Geological Society of Greece. 50, 383-391, https://doi.org/10.12681/bgsg.11739

[84] Shillington, D.J., McNeill, L.C., Carter, G.D.O. and the Expedition 381 Participants. 2018. Expedition 381 Preliminary Report: Corinth Active Rift Development. College Station, TX, International Ocean Discovery Program.

[85] Shillington, D.J., McNeill, L.C., Carter, G.D.O. and the Expedition 381 Participants. 2019. International Ocean Discovery Program Expedition 381 Preliminary Report. International Ocean Discovery Program; College Station: 1-36, https://doi.org/10.14379/iodp.pr.381.2019

[86] Singh, R., Kumar, R., Bahuguna, I.M. and Kumar, R. 2020. Grain Size Analysis of Dune and Bar Sediments of the Shyok River between Khalsar and Hunder Village, Karakoram Range, Ladakh, India. Journal of the Geological Society of India, 95, 183-189, https://doi.org/10.1007/s12594-020-1408-1

[87] Singh, M., Singh, I.B. and Mueller, G. 2007. Sediment characteristics and transportation dynamics of the ganga river. Geomorphology, 86, 144-175, https://doi.org/10.1016/j.geomorph.2006.08.011

[88] Sommerville, D, J.P., Mountney, N.P., Colombera, L. and Collier, R.E.Ll. 2019. Impact of a pre-existing transverse drainage system on active rift stratigraphy: An example from the Corinth Rift, Greece. Basin Research, 32, 764-788, https://doi.org/10.1111/bre.12396

[89] Styzen, M.J. 1997. Cascading Counts of Nannofossil Abundance. J. Nannoplankton Res. 19.

[90] Stefatos, A., Charalambakis, M., Papatheodorou, G. and Ferentinos, G. 2006. Tsunamigenic sources in an active

European half-graben (Gulf of Corinth, central Greece). Marine Geology, 232, 35-47, https://doi.org/10.1016/j.margeo.2006.06.004

[91] Sun, D.H., Bloemendal J., Rea, D.K., Vandenberghe, J., Jiang, F.C., An, Z.S. and Su, R.X. 2002. Grain-size distribution function of polymodal sediments in hydraulic and aeolian environments, and numerical partitioning of the sedimentary components. Sedimentary Geology, 152, 263-277, https://doi.org/10.1016/S0037-0738(02)00082-9

[92] Taylor, B., Weiss, J.R., Goodliffe, A.M., Maria, S., Mireille, L. and Alfred, H. 2011. The structures, stratigraphy and evolution of the Gulf of Corinth rift, Greece. Geophysical Journal International, 185, 1189-1219, https://doi.org/10.1111/j.1365-246X.2011.05014.x

[93] Tyler, S.W. and Wheatcraft, S.W. 1992. Fractal Scaling of Soil Particle-Size Distributions: Analysis and Limitations. S oil Science Society of America Journal, 56, 362-369, https://doi.org/10.2136/sssaj1992.03615995005600020005x

[94] Woodford, A.O. 1933. Origin and environments of source sediments of petroleum Paker D. Trask. The Journal of Geology, 41, 444-445, https://doi.org/10.2307/30058975

[95] Udden, J.A. 1914. Mechanical composition of clastic sediments. GSA Bulletin, 25, 655-744, https://doi.org/10.1130/GSAB-25-655

[96] Udden, J.A. 1898. Mechanical composition of wind deposits. Augustana Library Publications, 8, 838-839, https://doi.org/10.1126/science.8.206.838.b

[97] Visher, G.S. 1969. Grain-size distributions and depositional processes. Journal of Sedimentary Research, 39, 1074-1106, http://jsedres.sepmonline.org/cgi/doi/10.1306/74D71D9D-2B21-11D7-8648000102C1865D

[98] Watkins, S.E., Whittaker, A.C., Bell, R.E., Brooke, S.A.S., Ganti, V., Gawthorpe, R.L., McNeill, L.C. and Nixon, C.W. 2020. Straight from the source's mouth: Controls on field-constrained sediment export across the entire active Corinth Rift, central Greece. Basin Research, 32, 1600- 1625, https://doi.org/10.1111/bre.12444

[99] Wentworth, C.K. 1922. A scale of grade and class terms of clastic sediments. The Journal of Geology, 30, 377-392, https://doi.org/10.1086/622910

[100] Weltje, G.J. and Tjallingii, R. 2008. Calibration of XRF core scanners for quantitative geochemical logging of sediment cores: theory and application. Earth and Planetary Science Letters, 274, 423-438, https://doi.org/10.1016/j.epsl.2008.07.054

[101] Xiao, S.B., Li, A.C., Liu J.P., Chen, M.H., Xie, Q., Jiang, F.Q., Li, T.G., Xiang, R. and Chen, Z. 2006. Coherence between solar activity and the East Asian winter monsoon variability in the past 8000 years from Yangtze River-derived mud in the East China Sea. Palaeogeography Palaeoclimatology Palaeoecology, 237, 293-304, https://doi.org/10.1016/j.palaeo.2005.12.003

[102] Xiao, S.B. and Li, A.C. 2005. A study on environmentally sensitive grain-size population in inner shelf of the East China Sea (in Chinese with English abstract). Oceanologia et Limnologia Sinica, 23, 27-34.

[103] Yuan, J., Yang, X.J., Lu, Z.Y., Chen, W.J., Fan, H.L. and Yuan, L.R. 2011. Probability cumulative grain-size curves in sandy conglomerate of the upper Es4 in Yan22 block, Dongying depression (in Chinese with English abstract). Acta

Sedimentologica Sinica, 29, 815-524.

[104] Zhang, T.L., Wang, R.J., Xiao, W.S., Polyak, L., Astakhov, A., Dong, L.S., Wang, C.J., Liu, Y.G. and Shi, X.F. 2021. Characteristics of terrigenous components of Amerasian Arctic Ocean surface sediments: Implications for reconstructing provenance and transport modes. Marine Geology, 437, 106497, https://doi.org/10.1016/j.margeo.2021.106497

[105] Zhong, S.J. and Mucci, A. 1989. Calcite and aragonite precipitation from seawater solutions of various salinities: Precipitation rates and overgrowth compositions. Chemical Geology, 78(3-4): 283-299, https://doi.org/10.1016/0009-2541(89)90064-8

[106] Zulhikmah, Yuskar, Y., Putra, P.S., Nugroho, S.H. and Choanji, T. 2020. Characteristics of Quaternary Deep Sea Sediment in the Sumba Strait based on Grain Size and LoI (Lost on ignition Analysis). IOP Conference Series: Materials Science and Engineering. 797, 012004, https://doi.10.1088/1757-899X/797/1/012004

Figure Captions

Fig. 1. General structure and geography of the Corinth Rift. (a) Location and tectono-sedimentologica map of the Gulf of Corinth. The red dot shows the location of site M0079A. The red dashed line shows the location of profile in b. Part of the tectono-sedimentological of the Corinth rift during the Late Pleistocene from Gawthorpe et al. (2018). Drainage reversal from Ford et al. (2016). NAF, North Anatolian Faul; KF, Kephalonia Fault. (b) Map of the N-S seismic features through site M0079A. Interpretations from Nixon et al. (2016) (faults from the authors' own mapping). Unit 1 is older, generally non-reflective and poorly stratified (Bell et al. 2009). Unit 2 is younger, stratified and cyclical (Bell et al. 2009). The estimated age of the unit 1/2 unconformity of ca. 0.6 Ma (Bell et al., 2008; Nixon et al., 2016). Inset: seismic line and drill site locations.

Fig. 2. X-ray fluorescence (XRF) calibration workflow. (a) A log-ratio calibration (LRCE) approach (Weltje & Tjallingii, 2008) was employed to obtain optimum log-ratio denominator (in this case 'Ca'). The concentration of 5 elements (Ca, Fe, Mg, Mn and Sr) was selected in 16 ground sediment samples. The Br element is not selected due to showing too low concentrations. (b) Intensity and concentration calibration of the log (Sr/Ca). (c) The detailed compositional profiles of the Sr element (expressed as intensity counts). (d) The calibrated log ratio profiles.

Fig. 3. The lithological column and geochemistry element curves with depth of the 249-323 mbsf intervals. Sr (strontium), Ca (calcium), Fe (iron), Mn (manganese), Br (bromine), Ca/Sr ratio, Ca/Fe ratio, and Ma/Ca ratio counts from the XRF core scanner (the curves of Br and Ca elements were expressed as intensity counts; the curves of light gray were calibrated log ration, and were expressed as dimensionless units). Black arrows and black dashed arrows indicate the curves changing trends. The data of columns A, B, and C were from McNeill et al. (2019). Column D (authors' own recognized from cores): Pho., *Phoebichnus*; Te., *Teichichnus*; Phy., *Phycosiphon*.

Fig. 4. The lithological column and geochemistry element curves with depth of the 540-630 mbsf intervals. Sr (strontium), Ca (calcium), Fe (iron), Mn (manganese), Br (bromine), Ca/Sr ratio, Ca/Fe ratio, and Ma/Ca ratio counts from the XRF core scanner (the curves of Br and Ca elements were expressed as intensity counts; the curves of light gray were calibrated log ration, and were expressed as dimensionless units). Black arrows, black dashed arrows and red arrows indicate the curves changing trends. The data of columns A, B, and C were from McNeill et al. (2019). Column D (authors' own recognized from cores): Pho., *Phoebichnus*; Te., *Teichichnus*; Phy., *Phycosiphon*.

Fig. 5. Core photographs from site M0079A showing examples of trace fossils. (a) Oblique transverse cross section through a radiating burrow of *Phoebichnus*. This radial burrow is approximately 1 cm in diameter. (b) In the core, *Phycosiphon* appears as tiny yellow spots (transverse section) and yellow lines (longitudinal section). (c) *Teichichnus* appears as a series of wavy, tightly packed, and long laminate in core sections.

Fig. 6. Discrimination of sedimentary provenance and frequency distribution curve. (a) The skewness-standard deviation diagram of core M0079A samples at study intervals; (b) Grain-size frequency distribution of core M0079A samples at study intervals.

Fig. 7. Standard deviation vs. grain-size of core M0079A samples at study intervals.

Fig. 8. The probability cumulative curves of core M0079A samples at study intervals.

Fig. 9. Core photographs from site M0079A showing examples of (a) example of two slumped beds (a-1: Core 129R-1, borehole depth 564.28-564.63 mbsf; a-2: Core 130R-3, borehole depth 570.33-570.54 mbsf), (b) Graded beds (b-1: Core 132R-2, borehole depth 580.04-580.21 mbsf; b-2: Core 141R-3, borehole depth 619.02-619.44 mbsf), which generated by weak and dilute flows, (3) Homogeneous muds (c-1: Core 71R-3, borehole depth 287.84-288.24 mbsf), and mud beds with continuous white laminations (c-2: Core 137R-1, borehole depth 600.21-600.61 mbsf).

Fig. 10. Left: grain-size curves with depth of the study section. Right: photograph of core and probability accumulation curve of the sampling point of hole M0079A, the criterion of probability accumulation curve refers to Visher (1969).

Fig. 11. Evolution of sedimentary environment, hydrodynamics, and provenance in the study area. Environment evolution from the authors' own analyses, see Figures 3 and 4. The evolution of weights of several controlling factors is used to represent the trend of change.

Fig. 12. Probability accumulation curve chart for distinguishing provenance and hydrodynamic in the study area.

Fig. 13. Schematic cross sections summarizing the hydrodynamic and provenance interpretations for the M0079A site for the Gulf of Corinth. (a) Gulf periodically sea-connected after drainage reversal of the south of the Gulf of Corinth. (b) Isolated lakes with intermittent marine incursions before drainage reversal of the south of the Gulf of Corinth. (c) Photomosaic of sedimentary sequences on the Corinth Isthmus. (d) The bidirectional ripples within fine sandstones. The lens cap is 6 cm in diameter.

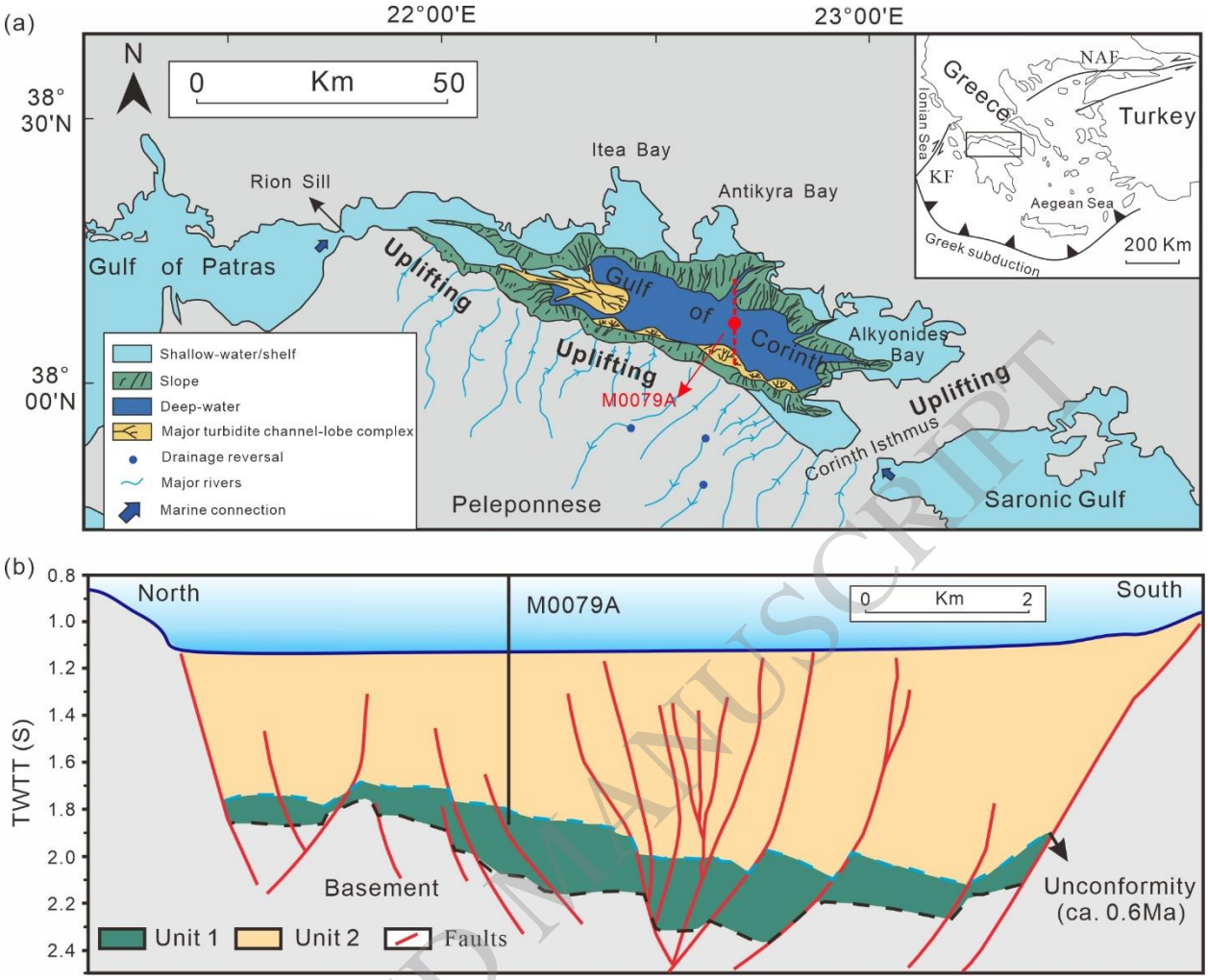

Figure 1

(a)

	Mg	Ca	Mn	Fe	Sr
Mg	0	0.987	0.976	0.208	0.839
Ca	0.987	0	0.998	0.986	0.995
Mn	0.976	0.998	0	0.999	0.189
Fe	0.208	0.986	0.999	0	0.372
Sr	0.839	0.995	0.189	0.372	0

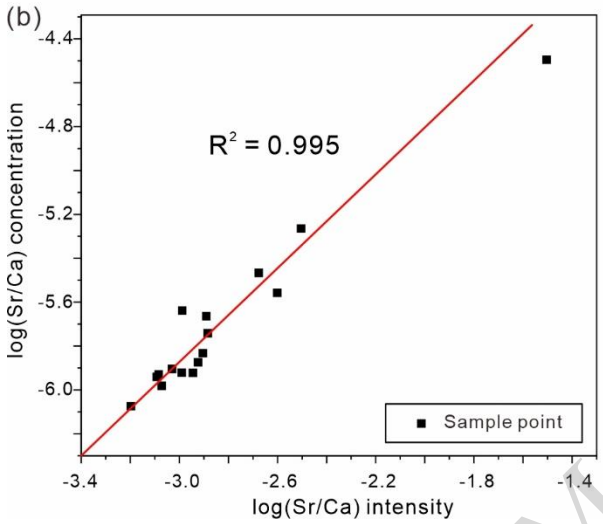

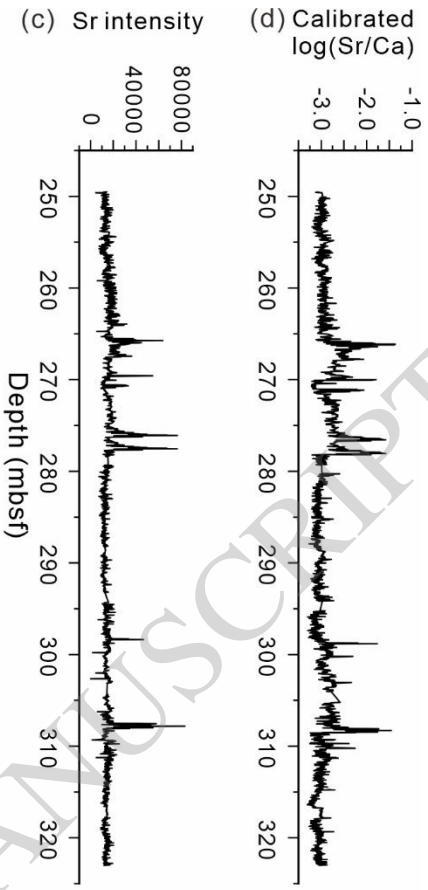

Figure 2

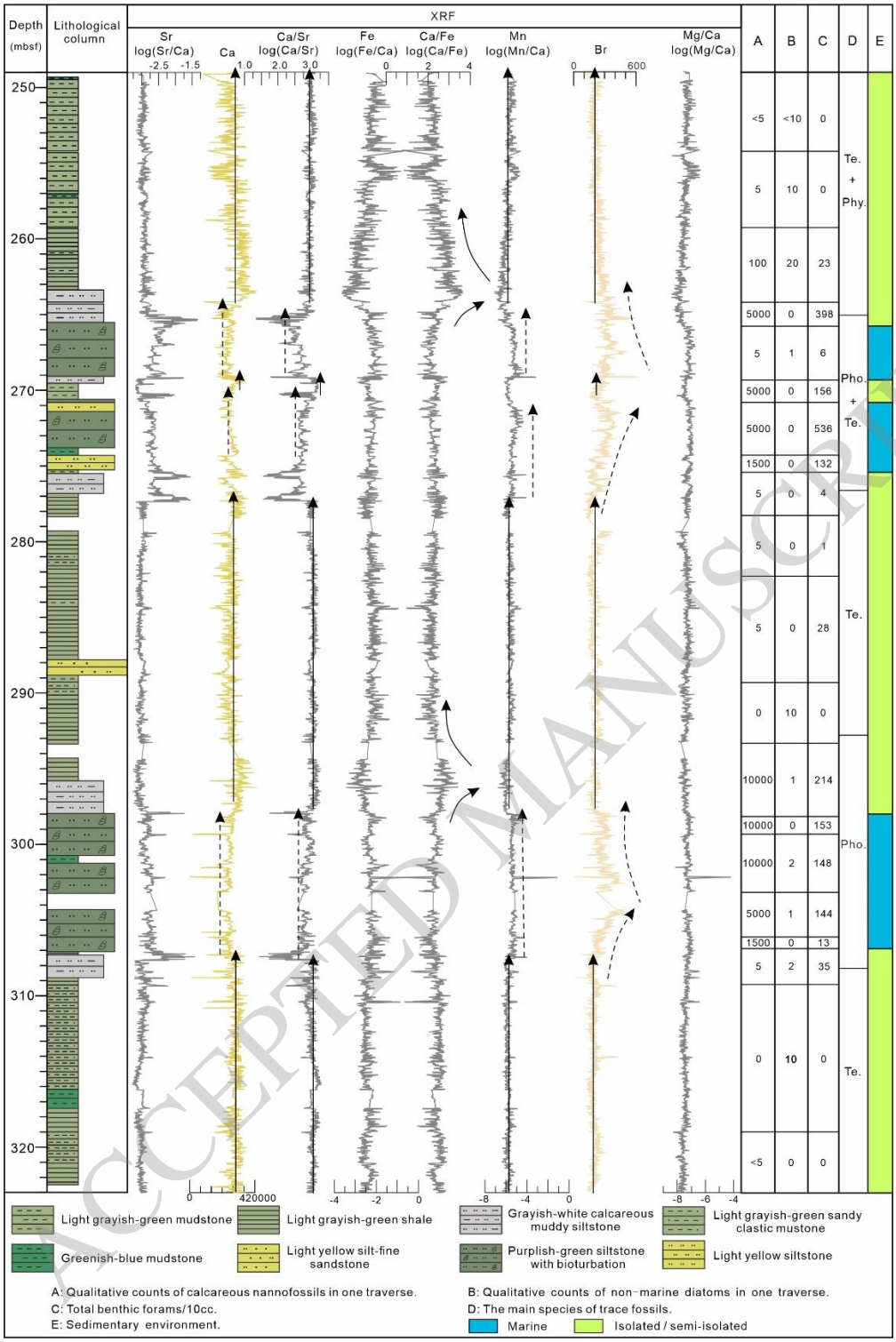

Figure 3

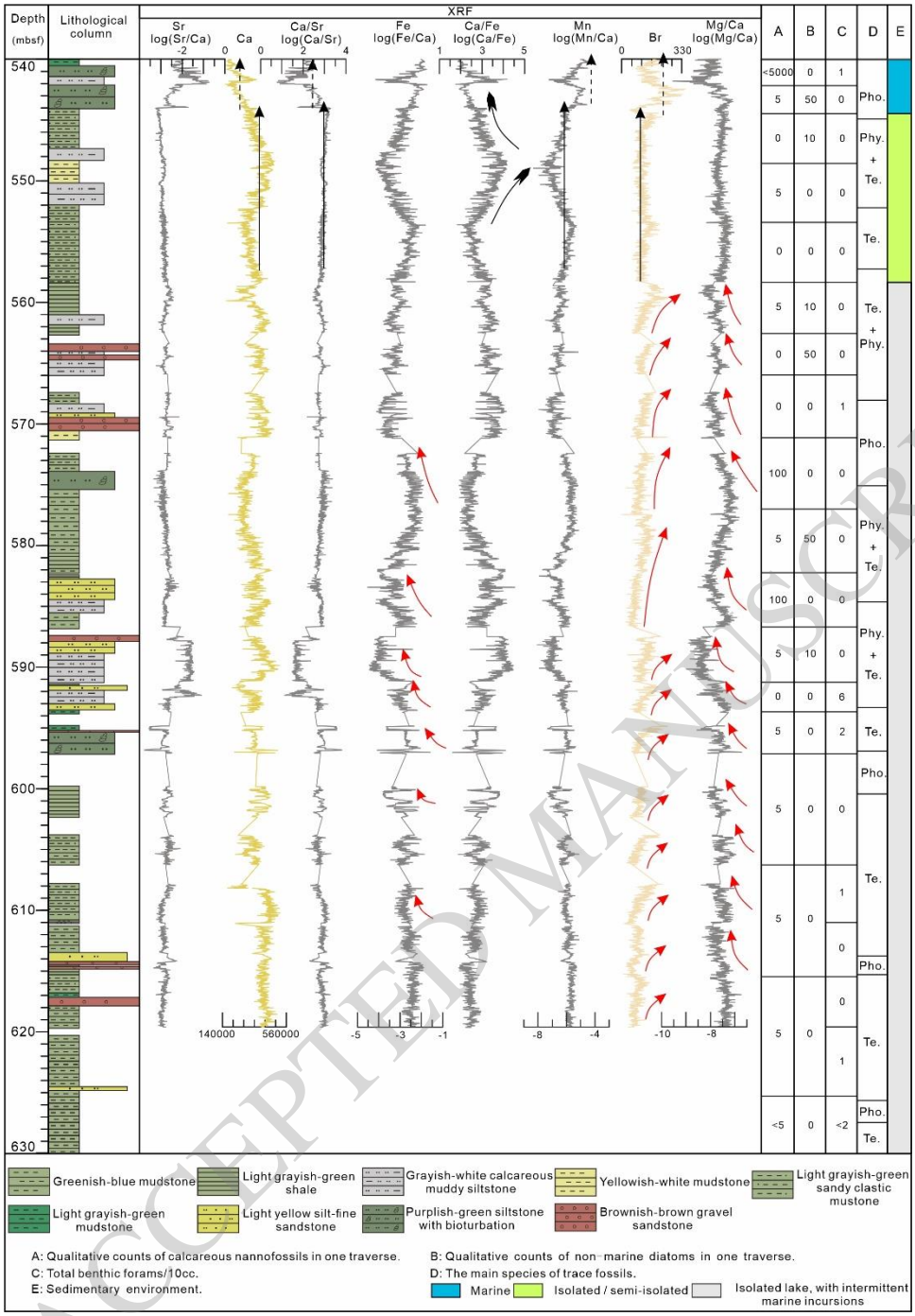

Figure 4

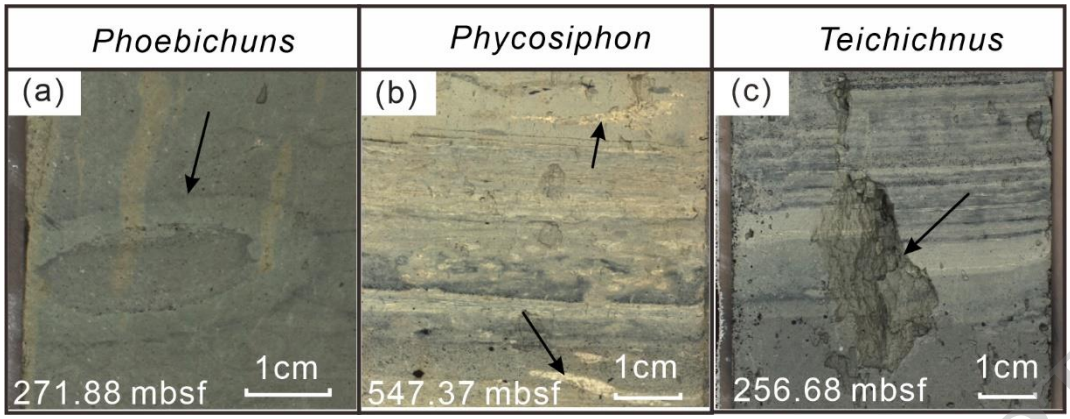

Figure 5

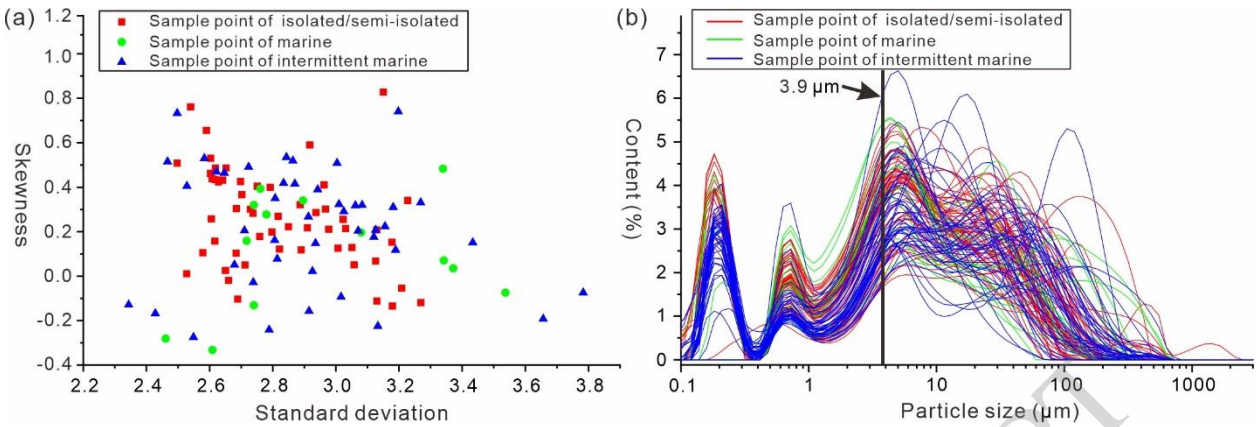

Figure 6

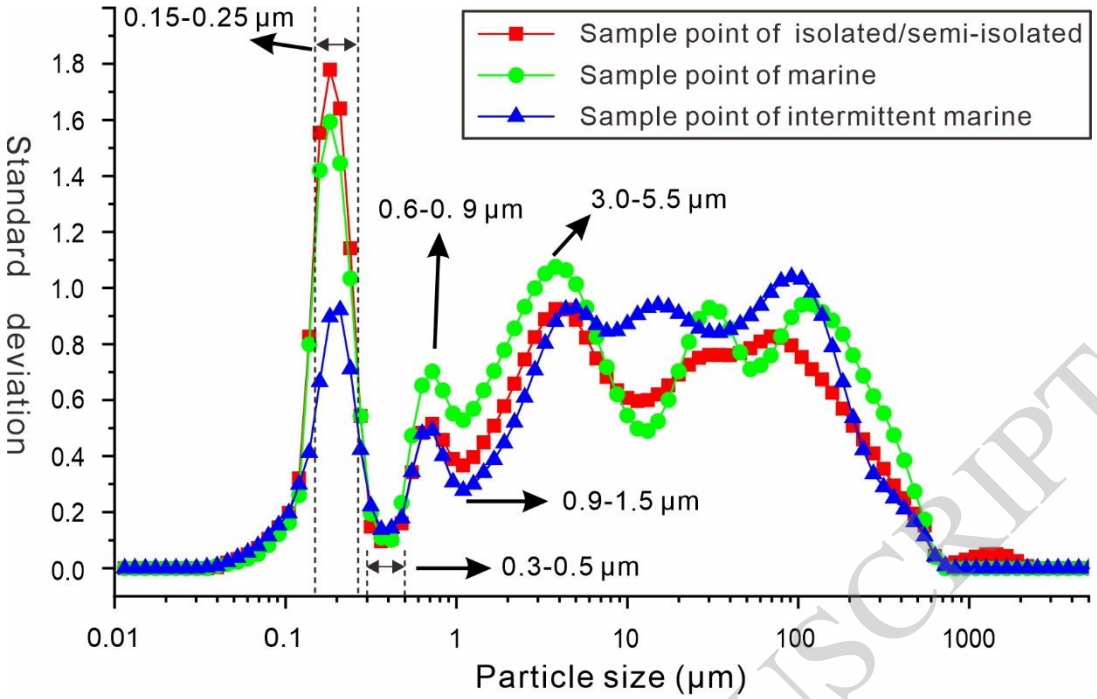

Figure 7

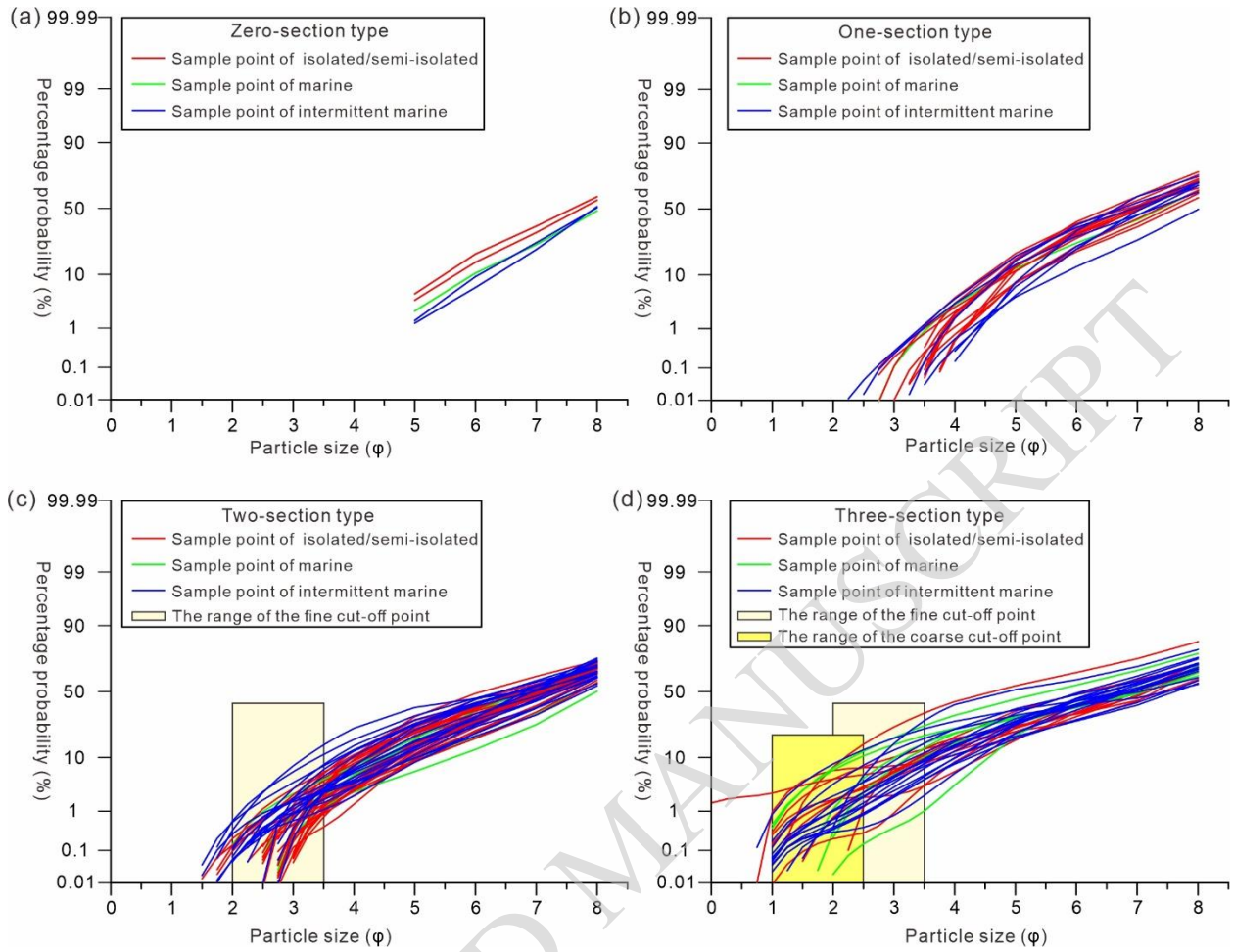

Figure 8

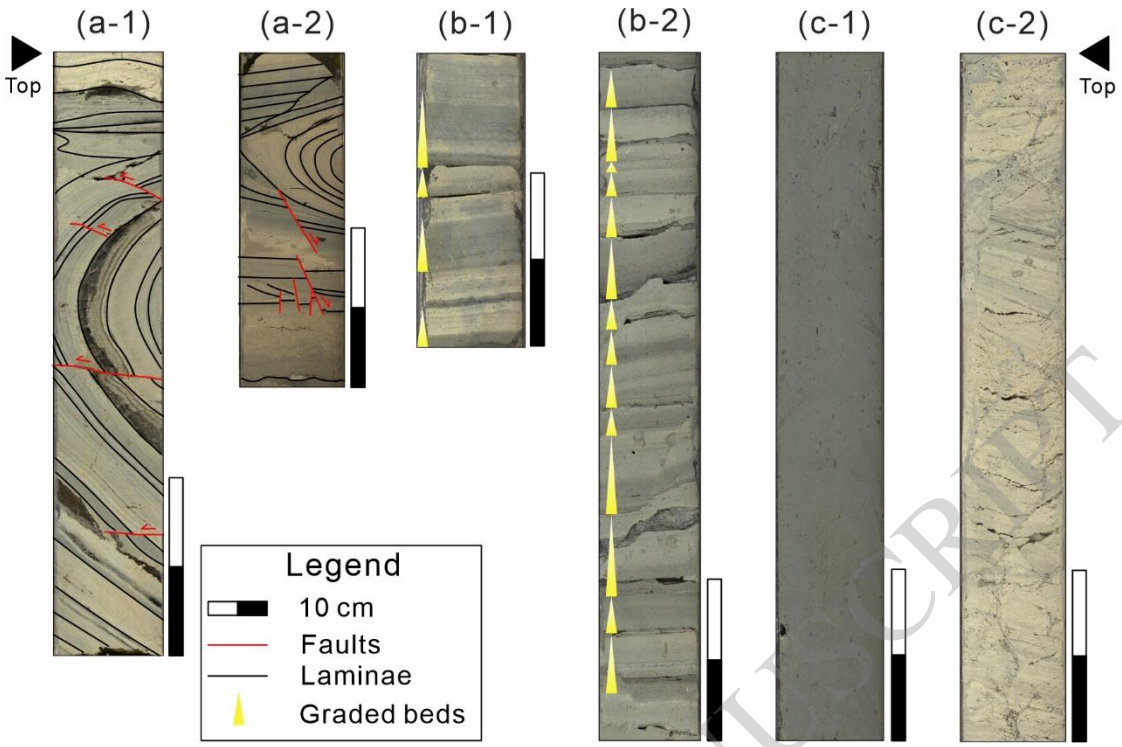

Figure 9

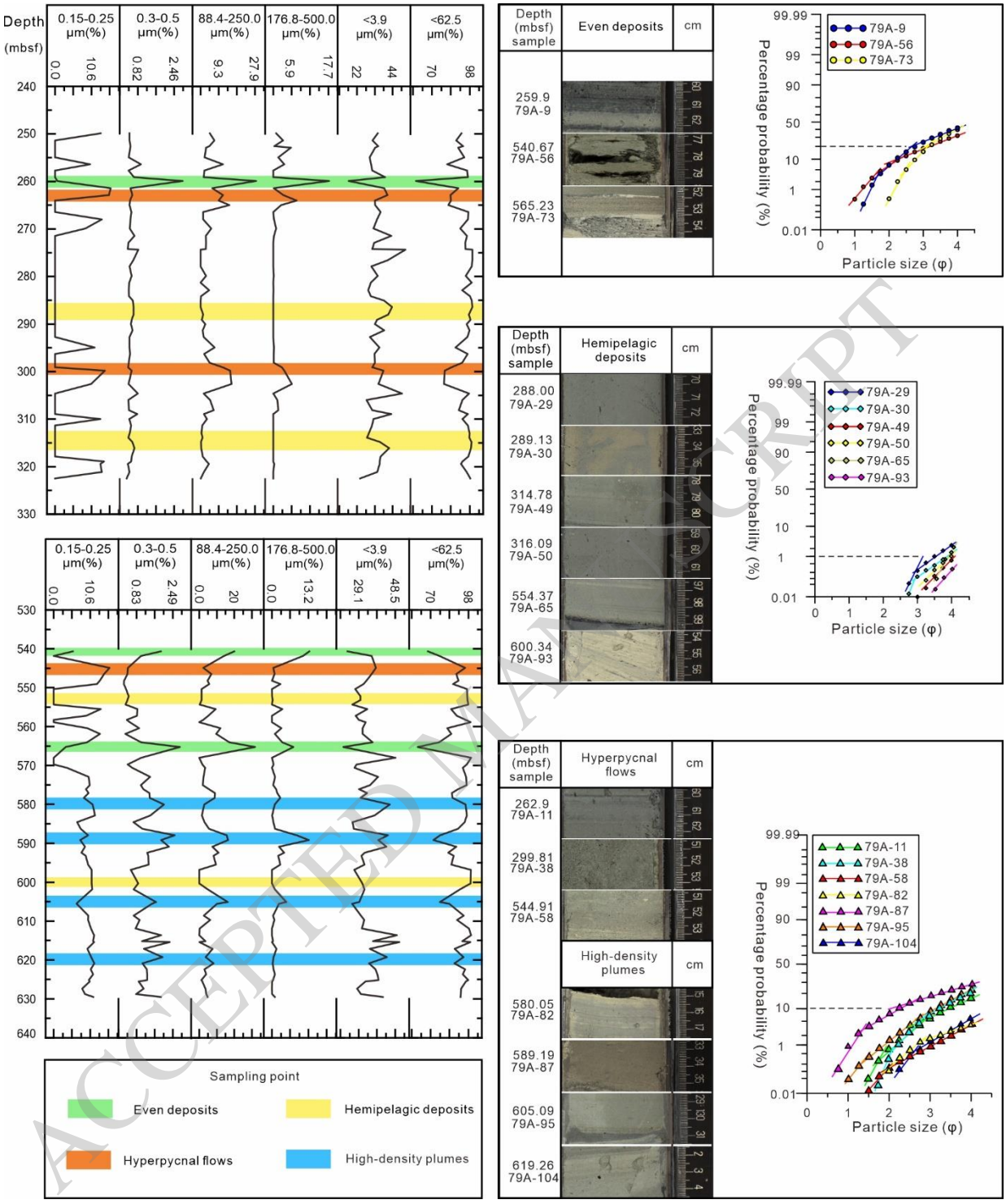

Figure 10

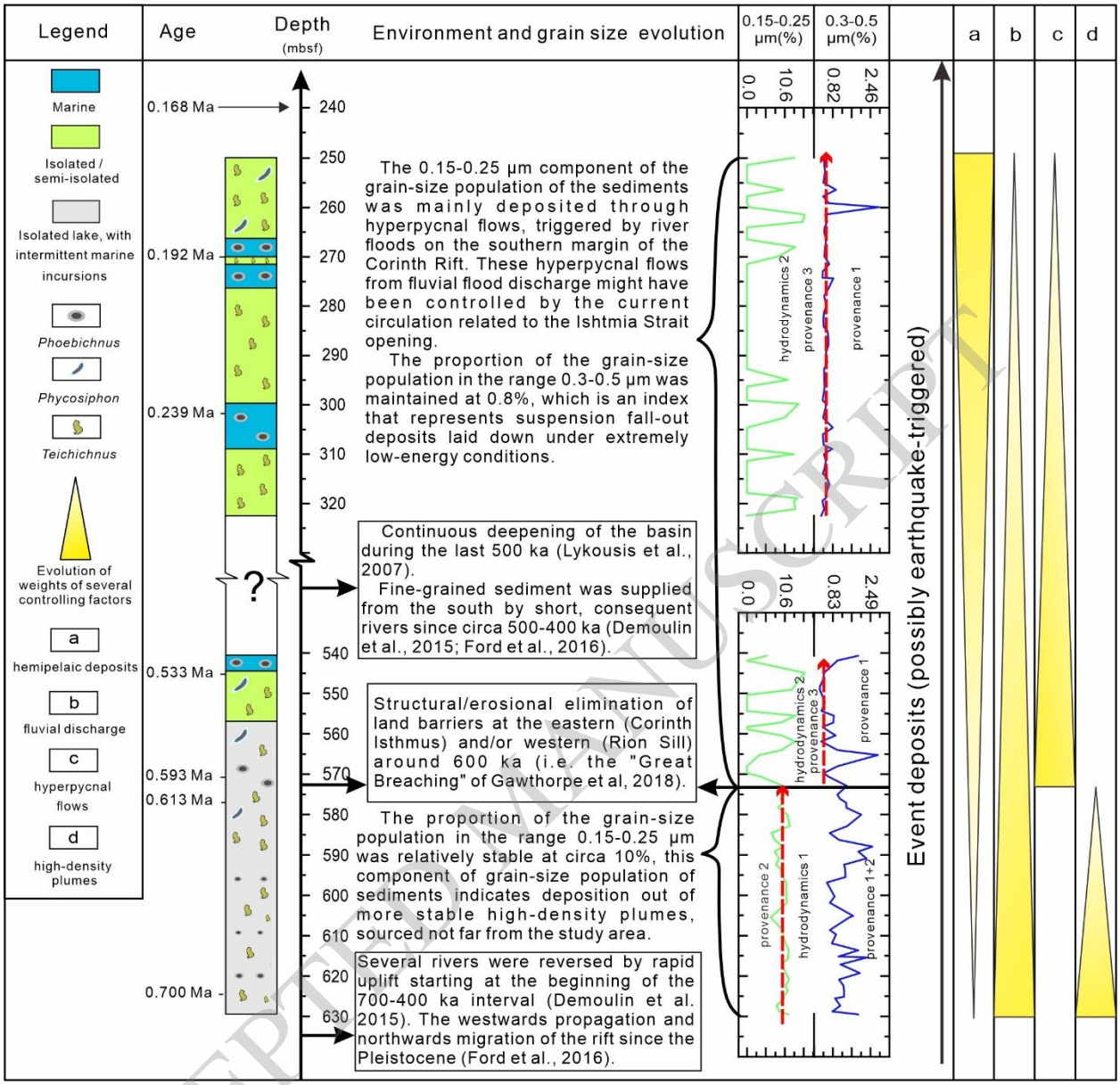

Figure 11

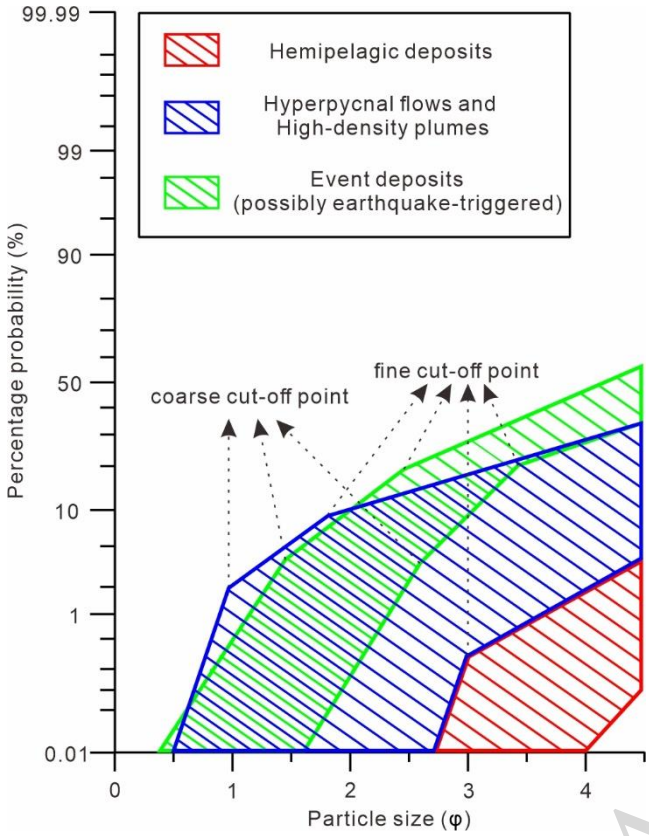

Figure 12

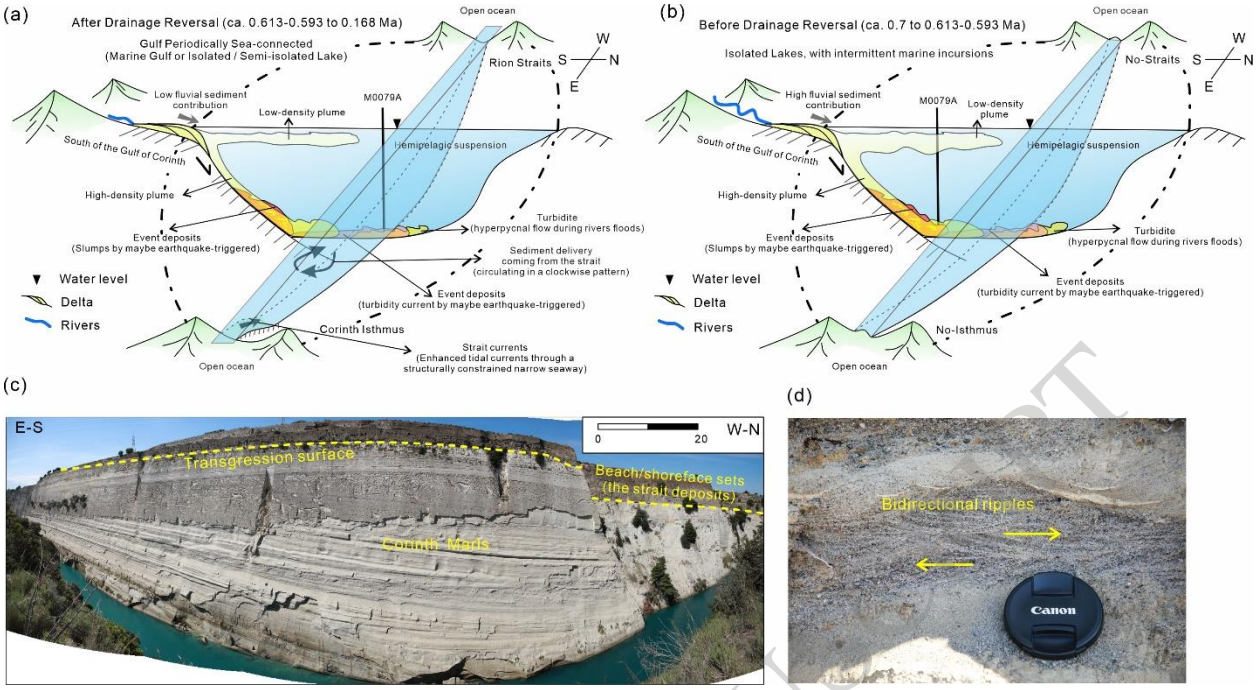

Figure 13